Integrating field, textural and geochemical monitoring to track eruption triggers and dynamics: a case-study from Piton de la Fournaise

Lucia Gurioli[1], Andrea Di Muro[2], Ivan Vlastélic[1], Séverine Moune[1], Simon Thivet[1], Marina Valer[1], Nicolas Villeneuve[2], ~~Patrick Bachèlery[1], Marina Valer[1], Simon Thivet[1],~~ Guillaume Boudoire[2,3], Aline Peltier[2], Patrick Bachèlery[1], Valerie Ferrazzini[2], Nicole Métrich[2], Mhammed Benbakkar[1], Nicolas Cluzel[1], Christophe Constantin[1], Jean-Luc Devidal[1], Claire Fonquernie[1], Jean-Marc Hénot[1]

(1) Université Clermont Auvergne, CNRS, IRD, OPGC, Laboratoire Magmas et Volcans, F-63000 Clermont-Ferrand, France

(2) Institut de Physique du Globe (IPGP), Sorbonne Paris-Cite, CNRS UMR-7154, Université Paris Diderot, Observatoire Volcanologique du Piton de la Fournaise (OVPF), Bourg Murat, France,

(3) Laboratoire Géosciences Réunion, Université de La Réunion, Institut de Physique du Globe de Paris, Sorbonne Paris-Cité, UMR 7154 CNRS, F-97715 Saint-Denis, France

Corresponding author: L Gurioli, Université Clermont Auvergne, CNRS, IRD, OPGC, LMV Campus Universitaire des Cézeaux 6 Avenue Blaise Pascal 63178 Aubière Cedex (lucia.guriolica.fr)

Abstract (250 words)

The 2014 eruption at Piton de ~~l~~La Fournaise (PdF), la Reunion, which occurred after 41 months of quiescence, began with surprisingly little precursory activity, and was one of the smallest so far observed at PdF in terms of duration (less than 2 days) and volume (less than 0.4 Mm^3). The pyroclastic material was composed of spiny-opaque, spiny-iridescent, and fluidal basaltic scoria along with golden basaltic pumice. Density analyses performed on 200 lapilli reveal that the spiny-opaque clasts are the densest (1600 kg/m^3) and richest in crystals (5~~5~~ vol%), and the golden pumices are the lightest (400 kg/m^3) and poorest in crystals (~~14~~ 8 vol%). The connectivity data indicate that the fluidal and golden (Hawaiian-like) clasts have more isolated vesicles (up to 40%) than the spiny (Strombolian-like) clasts (0-5%). These textural variations are linked to primary pre-eruptive magma storage conditions. The golden and fluidal fragments track the hotter portion of the melt, in contrast to the spiny fragments and lava ~~which~~ that mirror the cooler portion of the shallow reservoir. Exponential decrease of

the magma ascent and output rates corresponded to pProgressive tapping of these distinct portions of the storage system. Increasing syn-eruptive degassing and melt-gas decoupling leads to a decrease in the explosive intensity from early fountaining to Strombolian activity. The geochemical results confirm the absence of new hot input of magma into the 2014 reservoir and confirm the involvement emission of a single, shallow, differentiated magma source, possibly related to residual magma from the November 2009 eruption. Fast volatile exsolution and crystal-melt separation (second boiling) were triggered by deep pre-eruptive magma transfer and stress field change. Our study highlights the possibility that shallow magma pockets can be quickly reactivated by deep processes without mass or energy (heat) transfer and produce hazardous eruptions with only short term elusive precursors.We found that the eruption was triggered by water exsolution, favoured by the shallow depth of the reservoir, rather than cooling and chemical evolution of the stored magma.

Key words : Piton de La Fournaise, Hawaiian activity, Strombolian activity, shallow reservoire, texture, petrology, geochemistry

1. Introduction

A detailed characterization and understanding of eruptive dynamics and of processes driving and modulating volcano unrest is crucial in monitoring active volcanoes and fundamental for forecasting volcanic eruptions (Sparks, 2003). Many studies suggest that eruptive phenomena are strongly dependent on the physico-chemical properties of ascending magma in the conduit (e.g., temperature, viscosity, porosity, and permeability) (e.g. Sparks, 1978; Rust and Cashman, 2011; Gonnermann and Manga, 2013; Polacci et al., 2014). Integrating petrographic, chemical and textural data can thus provide critical information to constrain both the pre-eruptive storage conditions, and the processes related to magma ascent, degassing and cooling (e.g., reference in Table 1 in Gurioli et al., 2015). This multidisciplinary approach is of even greater importance in the monitoring of volcanoes which emit relatively unchanging magma compositions over time, like basaltic volcanoes (e.g. Di Muro et al., 2014; Gurioli et al., 2015; Coppola et al., 2017). As a result, monitoring of textures, and petrochemical properties of lava fragments and pyroclasts is now routinely carried out on a daily basis at active volcanoes such as Kilauea, Etna, and Stromboli (e.g., Thornber et al., 2003; Polacci et al., 2006; Swanson et al., 2009; Taddeucci et al., 2002; Colo' et al., 2010; Houghton et al., 2011; 2013; 2016; Carey et al., 2012; 2013; Lautze et al., 2012; Andronico et

2

al., 2013a; b; 2014; Corsaro and and Miraglia, 2014; Di Muro et al., 2014; Eychienne et al., 2015; Gurioli et al.; 2014; Leduc et al., 2015; Leibrandt and Le Pennec and Leibrandt, 2015; and Kahl et al., 2015). In the past, time series of petrographic and geochemical data have been measured for Piton de la Fournaise (PdF) basalts and particularly for effusive products. The aim of these datasets was to constrain potential time and space magma evolution for one of the most active basaltic volcanoes of the world (e.g. Albarède et al., 1997; Vlastélic et al., 2005; 2007, 2009; Vlastèlic and Pietruszka, 2016; Schiano et al., 2012; Boivin and Bachèlery, 2009; Peltier et al., 2009; Lénat et al., 2012; Di Muro et al., 2014; 2015). However, this type of approach has seldom been coupled with detailed textural studies at PdF and instead has mostly focused on crystal textures and crystal size distribution (Welsch et al., 2009; 2013; Di Muro et al., 2014; 2015). Moreover, only sporadic data exist on the textures of pyroclasts ejected by the PdF (Villemant et al., 2009; Famin et al., 2009; Michon et al., 2013; Vlastéelic et al., 2013; Welsch et al., 2009; 2013; Morandi et al., 20165; Di Muro et al., 2015; Ort et al., 2016).

Within this paper, we present a multidisciplinary textural, chemical and petrological approach to quantify and understand the short-lived 2014 PdF eruption. This approach combines detailed study of the pyroclastic deposit (grain_size and componentry) with bulk texture analysis (density, vesicularity, connectivity, morphology, vesicle distribution and crystal content) and a petro-chemical study (bulk rock, glass, minerals, melt inclusions) of the same clasts. This integrated approach has now been formalized within the National Observation Service for Volcanology (SNOV) as routine observational systems (DynVolc), Dynamics of Volcanoes, (http://wwwobs.univ-bpclermont.fr/SO/televolc/dynvolc/) and GazVolc, Observation des gaz volcaniques, ———(http://wwwobs.univ-bpclermont.fr/SO/televolc/gazvolc) to provide data for the on-going activity at PdF (Harris et al., 2017).

In spite of being the first of a series of eruptions, the June 2014 event was preceded by only weak inflation and by a rapid increase in number of shallow (< 2 km below volcano summit) volcano tectonic earthquakes that happened only 11 days before the eruption (Peltier et al., 2016). The eruptive event was dominantly effusive, lasted only 20 hours and emitted a very small volume of magma (ca. 0.4 Mm^3, Peltier et al., 2016), which makes this event one of the smallest, in terms of duration and volume, observed at PdF up to now. In addition, the eruption started during the night and very little direct observation exists for the first few hours of the activity, when the lava effusion was associated with very weak fountaining activity and

100 Strombolian explosions.

101   This eruption occurred just outside the southern border of the summit Dolomieu
102 caldera, at the top of the central cone of PdF (Fig. 1). This is a high risk sector because of the
103 high number of tourists. Identification of precursors of this kind of activity represents an
104 important challenge for monitoring systems (Bachélery et al., 2016).

105   Therefore this eruption represents an ideal context to apply our multidisciplinary
106 approach, with the aim of addressing the following key questions:

107   (i)   why was such a small volume of magma erupted instead of ~~forming an~~
108 ~~intrusion~~remaining intruded?

109   (ii)   what caused the rapid trigger and the sudden end to this small volume
110 eruption?

111   (iii)   which was the source of the eruption (shallow versus deep, single versus
112 multiple small magma batches)?

113   (iv)   what was the ascent and degassing history of the magma?

114   ~~(iii)~~(v) what was the time and space evolution of the eruptive event?

115 Furthermore, this eruption provides an exceptional opportunity to study processes leading to
116 the transition from mild Hawaiian (<20 m high fountains, following the nomenclature
117 proposed by Stovall et al., 2011) to Strombolian activity (<10 m high), whose products are
118 little modified by post-fragmentation processes because of the very low intensity of the
119 activity.

120   ~~Finally, with these results we want to stress how combined textural and petro-chemical~~
121 ~~quantification of the eruptive products can be used to characterize on going activity, and to~~
122 ~~provide valuable information to understand both the causes and the dynamics of potentially~~
123 ~~harmful eruptions.~~

124

125 **2 The 2014 activity**

126 **2.1 Precursory activity**

127 The 20 June 2014 summit eruption represents the first eruption at PdF after 41 months of
128 quiescence. The last ~~previous~~ eruption had been on 9 December 2010, with a shallow (above
129 sea level) intrusion on 2 February 2011 (Roult et al., 2012). From 2011, the deformation at
130 PdF was constant with two distinct types of behaviour: (i) a summit contraction of a few
131 centimetres every year (Fig. 1d); (ii) a preferential displacement of the east flank at a rate of
132 1-3 centimetres per year (Brenguier et al., 2012; Staudacher and Peltier, 2015). The

4

background microseismicity was very low (< 5 shallow events/day below volcano summit) and low-temperature summit intracaldera fumaroles emitted very little sulphur (H_2S or SO_2) and carbon (CO_2) (Di Muro et al., ~~2012;~~ 2016). After 41 months of rest, a new intense cycle of activity (June 2014, February 2015, May 2015, July 2015, August-October 2015; May 2016; September 2016; January 2017 and ~~the on-going eruption that had started the 14 of~~ July 2017) began with surprisingly little and ambiguous precursory activity.

The 2014 summit eruption started during the night of June 20/21, at 21h35 GMT (0h35 local time) and ended on June 21 at 17h09 GMT (21h09 local time), after less than 20 hours of dominantly effusive activity. The volcano reawakening was preceded, in March and April 2014, by deep (15-20 km below sea level) eccentric seismicity and increase in soil CO_2 flux below the western volcano flank, 15 km NW of the volcano summit (Liuzzo et al., 2015; Boudoire et al., 2017). Background microseismicity and inflation of the central cone increased progressively starting on 9 June 2014. Weak inflation recorded on both distal and summit baselines (Fig. 1d) suggest that deep (below sea level) magma up-rise was pressurizing the shallow (above sea level) magma storage system (Peltier et al., 2016). On June 13, 17 and 20, three shallow (hypocentres located above sea level) intense seismic crises occurred below the summit Dolomieu caldera (Fig. 1), with hundreds of events located in a narrow depth range between 1100 and 2100 metres below the volcano summit. These seismic crises consisted of swarms of low magnitude (M: 1-2) volcano tectonic events which increased in number from the first to the third crisis. On June 20, seismicity increased progressively and a final seismic crisis started at 20h20 GMT, only 75 minutes before the eruption. This last seismic crisis was coupled with acceleration in the deformation of the summit area, which began only 60 minutes before the eruption. Interestingly, only slight inflation of the central cone (< 2 cm of dilatation) was detected 11 days before the 2014 eruption with a maximum of 1 cm and 1.6 cm enlargement at the summit and the base of the cone, respectively (Peltier et al., 2016). A moderate increase in CO_2 and H_2S emissions from summit intracaldera fumaroles was detected starting on June 2, but only very minor SO_2 emissions occurred before the eruption (mostly on June 7 and 15, unpublished data). Therefore, the ~~increase~~ acceleration in both geophysical and geochemical parameters was mostly related to the late phase of injection of the dyke towards the surface just before the eruption. Following the end of the June 20-21 eruption, a long-term continuous inflation of the edifice began, at a moderate rate, and mostly at the base of the volcano. More than one year after this first eruption, the long-term deformation trends showed that the 2014 eruption marked a kink between the deflation trend

5

which followed the caldera-forming 2007 eruption (Staudacher et al., 2009) and the currently ongoing continuous inflation trend (Fig. 1d, and Peltier et al., 2016; Coppola et al., 2017).

2.2 Chronology of the events and sampling strategies

We reconstructed the chronology of events by combining a distribution map of the fissures, pyroclastic deposits and lava flows (Fig. 1) with a review of available images (visible and IR) and videos extracted from the observatory data base, the local newspapers, and web sites (Fig. 2). The 2014 eruption occurred at the summit and on the SE slopes (Figs. 2a and 2b) of the central cone and evolved quickly and continuously over 20 hours. The full set of fractures opened during a short period of time (minutes) and emitted short (<1.7 km long) lava flows (Fig. 1 and Figs. 2c and 2d). Feeding vents were scattered along a 0.6 km long fissure set (Fig. 1) and produced very weak (low) Hawaiian to Strombolian activity (Fig. 2).

Fissures opened from west to east, initially sub-parallel to the southern border of Dolomieu caldera and then propagated at lower altitude (Fig. 1). The summit part of the fractures (ca. 2500 m asl, Western Fracture, Fig. 1) emitted only small volumes of lava and pyroclasts. This part of the fracture set was active only during the first few hours of the eruption, at night. The eastern part of the fractures (Upper Fracture, Fig. 1) descended to lower altitude (between 2400 and 2300 m asl, Middle Fracture, Fig. 1) along the SE flank of the summit cone and emitted most of the erupted volume (Figs. 2a and 2b). As often observed in PdF eruptions, the activity progressively focused on a narrow portion of the fractures at low altitude and finally on a single vent located at the lower tip of the fracture system (Main Vent, at 2336 m asl, Figs. 1, 2). The first in situ observations in the morning of June 21 (ca. 04h00 GMT) showed that weak Strombolian activity (Figs. 2a and 2b) was focused on a narrow segment of the lower fractures and that a'a lavas had already attained the elevation of 1983 m asl (0.2 km before maximum runout, Fig. 2c). A small, weak gas plume was also blowing northwards. A single sample of partially molten lava was collected from the still active lava front and partially water quenched (Reu140621-1, Table S1, Fig. 2d). During most of June 21, the activity consisted of lava effusion in three parallel lava streams (Fig. 2c) merging in a single lava flow (Fig. 2e) and mild-weak "Strombolian" explosions at several closely spaced spots along the lower part of the feeding fracture. At 13.00 (GMT), only weak explosions were observed within a single small spatter cone (Figs. 2fe and 2gf). Most of the lava field was formed of open channel a'a lavas. The total volume of lava was estimated by MIROVA service (https://www.sites.google.com/site/mirovaweb/home), with the use of the MODIS

images and the analyses of the flux from the spectral properties, to be within 0.34 (+/- 0.12) million m^3 (Mm^3), (Coppola et al., 2017). Satellite derived volume estimates are consistent with independent photogrammetric estimates (0.4 ± 0.2 Mm^3; Peltier et al., 2016) and rank the 2014 eruption at the lower end of the volume range typically emitted by Piton de la Fournaise (Roult et al., 2012).

~~Apart from the sample from the front of the still active lava flow, all other samples were collected in two phases: 3 days after the eruption (pyroclasts on June 24, Fig. 3a; lavas on July 2) and three months later (pyroclasts from the Main Vent; November 18) (Table S1). June 24 samples were collected both from the main fractures, the Main Vent and the active lava flow (Fig. 1 and Table S1). Scattered scoriaceous bombs and lapilli were collected from the discontinuous deposits emplaced close to the Western Fracture, active only at the beginning of the eruptive event (Figs. 3c and 3d). In contrast, the sustained and slightly more energetic activity at the lower tip of the fractures built a small spatter cone and accumulated a small volume of inversely graded scoria fallout. This deposit is 10 cm thick at 2 m from the vent and covers an area of about ~1000 m² (Main Vent, Fig. 1). For this fall deposit we collected two bulk samples, one from the base (within the lower 5 cm) and the other from the top (within the upper 5 cm), for the grain size and componentry analyses. The sample at the base was collected in November because on June 24 the loose proximal lapilli blanket was still very hot (405 °C; thermocouple measurement, Fig. 3a) and fumaroles with outlet temperatures in the range 305-60 °C were observed all along the fractures several weeks after the eruption. Both in June and in October, more than 200 clasts of similar size (maximum diameter between 16 and 32 mm, see Gurioli et al. 2015) were collected, both close to the Main Vent and in the 'distal' area (30 metres away from the vent) for density, connectivity, permeability, petrological and geochemical analysis.~~

3. Methodology

3.1 Sampl~~ing~~**e strategy**

Apart from the sample from the front of the still active lava flow (Fig. 2d), all other samples were collected in two phases: 3 days after the eruption (pyroclasts on June 24, Fig. 3a; lavas on July 2) and three months later (pyroclasts from the Main Vent, on November 18) (Table S1). June 24 samples were collected both from the main fractures (WF and UF, Fig. 1a), the Main Vent and the active lava flow (Fig. 1 and Table S1). Twenty five scoriaceous bombs and lapilli (Reu140624-9a-1 to Reu140624-9a and Reu140624-9b-6 to Reu140624-9b-25, in Table

7

S3) were collected from the discontinuous deposit (Fig. 3d) emplaced at the Western Fracture site (Fig. 1a), active only at the beginning of the eruptive event. Because of the short duration of the activity at the WF, the scoria fragments on the ground were scarce (Fig. 3c). The strategy was to collect a sample that was formed by the largest available number of clasts that was representative of this discrete deposit (Reu140624-9 in Table S1). From the Upper fracture (UP in Fig. 1a) only one big scoria was collected (Reu140624-13, Table S1) that broke in five parts, allowing us to measure its vesiculated core and the dense quenched external part (Reu140624-13-a to Reu140624-13-e, in Table S3). In contrast, the sustained and slightly more energetic activity at the lower tip of the fractures built a small spatter cone (Fig. 2) and accumulated a small volume continuous deposit (Fig. 3a) of inversely graded scoria fallout (Figs. 3b). This deposit is 10 cm thick at 2 m from the vent and covers an area of about ~1000 m^2 (Main Vent, Fig. 1). For this fall deposit we collected two bulk samples, one from the base (within the lower 5 cm, Reu141118-6 in Table S1) and the other from the top (within the upper 5 cm, Reu140624-3, in Table S1), for the grain size and componentry analyses. The sample at the base was collected in November because on June 24 the loose proximal lapilli blanket was still very hot (405 °C; thermocouple measurement, Fig. 3a) and fumaroles with outlet temperatures in the range 305-60 °C were ~~observed~~sampled all along the fractures several weeks after the eruption (Fig. 1b and Table 1). These latter geochemical data are not presented in this paper. We selected 103 fragments from the coarse grained bulk deposit at the top of the Main Vent (Reu140624-3-1 to Reu140624-3-103, in Table S3) for density, connectivity, permeability, petrological and geochemical analysis. In addition, in November 2014, more than 200 clasts (comprising in the Reu141118-1 to Reu141118-5 samples, Table S1) of similar size (maximum diameter between 16 and 32 mm, see Gurioli et al., 2015) were collected, both close to the Main Vent and in the 'distal' area (30 metres away from the vent) to complete the particle bulk texture analyses and the chemical analyses.

3.2~~1~~ Grain size, componentry and ash morphology

We performed grain size analyses on the two bulk samples collected from the Main Vent, following the procedure of Jordan et al. (2015) (Table S2). The samples were dried in the oven at 90°C and sieved at ½ phi intervals in the range of -5 φ to 4 φ (Fig. 3c); the data are also shown in full phi for comparison with the deposits of the 2010 PdF fountaining episode (Hibert et al., 2015; Fig. 3f). Sieving was carried out by hand and for not longer than three minutes to avoid breaking and abrasion of the very vesicular and fragile clasts. For the scattered scoria sampled from the Western Fracture (Figs. 1, 3d~~e~~ and 3e~~d~~), we followed the

grain size strategy proposed in Gurioli et al. (2013). Within this procedure we sampled each fragment and we recorded the weight and the three main axes (a being the largest, b, and c). To allow comparison with the sieving grain size analyses (Inman, 1952), we used the intermediate b axis dimension to obtain $\varphi = -\log_2 b$.

Following the nomenclature of White and Houghton (2006) the componentry analysis is the subdivision of the sample into three broad components: i) juvenile, ii) non-juvenile particles, and iii) composite clasts. The juvenile components are vesicular or dense fragments, as well as crystals, that represent the primary magma involved in the eruption; non-juvenile material includes accessory and accidental fragments, as well as crystals that predate the eruption from which they are deposited. Finally, the composite clasts are mechanical mixtures of juvenile and non-juvenile (and/or recycled juvenile) clasts. In these mild basaltic explosions, the non-juvenile component is very scarce, so we focused on the juvenile component that is characterized by three groups of scoria: (i) spiny-opaque, (ii) spiny-glassy, and (iii) fluidal, along with golden pumice (Fig. 4). The componentry quantification was performed for each grain size fraction between -5 φ to 0.5 φ (Figs. 5a and 5b), where a binocular microscope was used for the identification of grains smaller than -1 phi (Table S2). ~~For the coarse ash fraction (250-300 μm size) of the two bulk deposits collected at the Main Vent, we also performed a morphological quantification using the Morphologi G3 at Laboratoire Magmas et Volcans (LMV) of Clermont Ferrand following the procedure of Leibrandt and Le Pennec (2015) to distinguish between smooth versus spiny clasts within the coarse ash (Fig. 5c).~~

In the following, we will use the crystal nomenclature of Welch et al. (2009), with the strictly descriptive terms of macrocrysts (> 3 mm in diameter) mesocrysts (from 0.3 to 3 mm in diameter), and microcrysts (<0·3 mm in diameter).

3.3~~2~~ Particle bulk texture (density, porosity, connectivity) and microtexture

For each sample site (WF, UF and Main Vent, Fig. 1a), we selected ~~27 to 146 juvenile~~ all the available particles within the 8-32 mm fraction for density and pycnometry measurements (Table S3). This is the smallest granulometric fraction assumed to be still representative of the larger size class in terms of density (Houghton and Wilson, 1989; Gurioli et al., 2015), and has been used in previous textural studies (e.g., Shea et al., 2010). In addition, this size range is ideal for vesicle connectivity measurements (e.g. Formenti and Druitt, 2003; Giachetti et al., 2010; Shea et al., 2012; Colombier et al., 2017a, b). Textural measurements (density/porosity, connectivity and permeability) were performed at the LMV. Density of

9

juvenile particles was measured by the water-immersion technique of Houghton and Wilson (1989), which is based on Archimedes principle. A mean value for the vesicle-free rock density was determined by powdering clasts of varying bulk densities, measuring the volumes of known masses using an Accupyc 1340 Helium Pycnometer, then averaging. The same pycnometer was also used to measure vesicle interconnectivity for each clast using the method of Formenti and Druitt (2003) and Colombier et al. (2017a). Permeability measurements were performed on five clasts: two golden pumices, one fluidal, one spiny glassy and one opaque scoriae, all collected from the Main Vent (Table S3). Following Colombier et al. (2017a), the clasts were cut into rectangular prisms to enable precise calculation of the cross-sectional area, which is required to calculate permeability. These prisms were then embedded in a viscous resin, which was left to harden for 24 h. The sample surface had been previously coated with a more viscous resin and then wrapped with parafilm to avoid intrusion of the less viscous resin inside the pores. The coated samples were placed with a sample holder connected to a permeameter built in Clermont-Ferrand following Takeuchi et al. (2008).

Vesicle size distribution and crystal content wasere performed following the method of Shea et al. (2010) and Leduc et al. (2015), while the total crystallinity, the percentages for both crystal phases (plagio and clinopyrox) and size-populations (meso and microcrysts) were calculated using the raw data from FOAM program (Shea et al 2010) and the CSDcorrections program of Higgins (2000) and the CSDslice data base (Morgan and Jerram 2006) to have the percentage in 3D. We performed these analyses on nine eight clasts picked up from each component-density distribution mode (stars in Figs. 6c6a and 6b). The choice of the clasts was made mostly on the typologies, rather than on each density distribution, in order to avoid the analysis of clasts with transitional characteristics. For example, two golden pumice fragments were selected from the largest clasts that were the less dense and didn't break, even if the values in vesicularity were similar. A larger number of fluidal fragments were chosen (even if the density distribution was unimodal) because this typology of clasts was the most abundant and was emitted all along the active fracture, so we did our best in order to study products representative of the Western Fracture, the Upper Fracture and the Main Vent activities. Only one spiny glassy and one spiny opaque were selected, because they were emitted only at the Main Vent. These data are presented in Figure 4 and we followed the strategy of Leduc et al. (2015) for the quantification of the vesicle size distribution.

A full description of ~~the protocol for~~ the ~~density and connectivity~~ textural measurements, ~~is available at , while the textural data are~~as well as the raw data of these measurements are available at DynVolc Database (2017).~~-~~

3.~~4~~3 Bulk geochemistry

For the determination of the bulk chemistry (Table S4 and Fig. 7) of the different pyroclasts we selected the largest pyroclasts of golden pumice and the largest fluidal, spiny glassy and spiny opaque scoriae (Table S4). We also analyzed two fragments of lava, from the beginning and the end of the eruption (Table S4). Samples were crushed into coarse chips using a steel jaw crusher and powdered with an agate mortar. Major and trace element compositions were analyzed using powder (whole rock composition). In addition, for a sub-set of pyroclasts, glass chips (2-5 mm in size) were hand-picked under a binocular microscope and analyzed separately for trace elements. For major element analysis, powdered samples were mixed with $LiBO_2$, placed in a graphite crucible and melted in an induction oven at 1050 °C for 4.5 minutes, resulting in a homogeneous glass bead. The glass was then dissolved in a solution of deionized water and nitric acid (HNO_3), and finally diluted by a factor of 2000. The final solutions were analyzed by ICP-AES. Trace element concentrations were analysed following a method modified from Vlast~é~elic et al. (2013). About 100 mg of sample (powder and chip) were dissolved in 2 ml of 28M HF and 1 ml of 14M HNO_3 in teflon beaker for 36 hours at 70°C. Solutions were evaporated to dryness at 70°C. The fluoride residues were reduced by repeatedly adding and evaporating a few drops of concentrated HNO_3, before being fully dissolved in ca. 20 ml of 7M HNO_3. These solutions were diluted by a factor of 15 with 0.05M HF (to reach rock dilution factor of ca. 4000) and trace element abundances were determined by quadrupole ICPMS (Agilent 7500). The analyses were performed in plasma robust mode (1550 W). The reaction cell (He mode) was used to reduce interference on masses ranging from 45 (Sc) to 75 (As). The signal was calibrated externally (every 4 samples) with a reference basaltic standard (USGS BHVO-2) dissolved as for the samples and using the GeoRem recommended values (http://georem.mpch-mainz.gwdg.de/). For elements that are not well characterized in literature (As, Bi, Tl), or which show evident heterogeneity (e.g. Pb) in BHVO-2 powder, the signal was calibrated using the certified concentrations of a synthetic standard, which was also repeatedly measured. The external reproducibility (2σ

error) of the method is 6% or less for lithophile elements and 15% or less for chalcophile elements.

3.54 Glass and crystal chemistry

Spot analyses of matrix glass and crystal composition (Table S5) were carried out using a Cameca SX100 electron microprobe (LMV), with a 15 kV acceleration voltage of 4 nA beam current and a beam of 5 µm diameter for glass analyses. However, for the spiny opaque scoria, characterized by abundant crystals with rapid growth textures, a voltage of 8 nA beam current and a beam of 10 µm diameter were used. For this latter sample, 10 analyses per sample were performed due to the heterogeneity within the highly crystallised glass (Fig. 8a), while for the other samples 6 analyses per sample were enough to characterize the clean homogeneous glass. For crystal analysis, a focused beam was used. For the characterization of the meso- and micro-crysts, due to their small size, only two to three measurements were performed, one at the edge, one in the middle and one at the core of the crystals, to check for possible zonation.

3.65 Melt inclusions

Melt inclusions (MIs; Table S6, Figs. 8b and 9) were characterized in the olivine mesocrysts from the three groups of scoriae (fluidal, spiny glassy and spiny opaque), but not in the pumice group, because c. Crystals in the pumice group were too rare and small to be studied for melt inclusionsMIs.

Olivine crystals were handpicked under a binocular microscope from the 100– 250 and 250– 600 µm grain size fractions of crushed tephra. Crystals with MIs were washed with acetone, embedded in epoxy and polished individually to generate adequate exposure of the MIs for *in situ* electron probe microanalysis. The MIs are spherical to oblate in shape and range in size from 10 to 200 µm. Some of the MIs contain shrinkage bubbles but all of those studied are totally deprived of daughter minerals. Major elements were measured on a Cameca SX-100 microprobe at LMV (Table S6). For major elements, the larger MIs were analyzed with a spot diameter of 10-20 **µ**m and sample current of 8 nA, whereas the smaller MIs were analyzed with a beam of 5 **µ**m and a sample current of 4 nA. The results are given in Table S6, and analytical details and uncertainties are listed in Óladóttir et al. (2011) and Moune et al. (2012).

12

4 Results

4.1 Deposit texture (grain size, componentry, morphology) and petrological description of the samples

The pyroclastic deposits at the Western and Upper fractures sites (Fig. 1a) are formed by scattered homogeneous smooth fluidal (Figs. 3d) bombs and lapilli scoria. The average dimension of the fragments is around 4 cm (maximum axis) with bombs up to 10 cm and scoria lapilli up to 2 cm in size.

At the Main Vent, the reversely graded deposit is made up of lapilli and bombs, with only minor coarse ash (Fig. 3c). The lower 5 cm at the base are very well-sorted and show a perfect Gaussian distribution with a mode at 4 mm. In contrast, the grain size distribution of the upper 5 centimetres is asymmetrical with a main mode coarser than 22 cm and a second mode at 8 mm. This upper deposit is negatively skewed due to the abundance of coarse clasts. The dataset show a similarity between the grain size distributions of the basal tephra ejected from the 2014 main vent and the ones for the lava fountaining of the 2010 summit event (Hibert et al., 2015). On the contrary, the top of the 2014 fall differs from fountain deposits, being coarser and polymodal, and it is ascribed to dominantly Strombolian activity.

In terms of componentry of the deposits, four types of clasts were distinguished (Fig. 4): (i) golden pumice, (ii) smooth or rough fluidal scoriae, (iii) spiny glassy scoria, (iv) spiny opaque scoria. The pumices are vesicular, light fragments, characterized by a golden to light brown color, sometimes with a shiny outer surface (Fig. 4a). They are usually rounded in shape. Golden clasts studied for textures contain a few microcrysts of plagioclase (up to 0.1 mm in diameter), clinopyroxene up to 0.05-0.06 mm in diameter, and small olivine up to 0.03 mm in diameter (Fig. 4), together with large areas of clean, light brown glass. The fluidal scoria fragments have dark, smooth or rough shiny surfaces (Fig. 4b). They can be more or less elongated in shape and have spindle as well as flattened shapes. The fluidal fragments are characterized by rare mesocrysts of plagioclase and clinopyroxene and microcrysts of plagioclase, clinopyroxene and olivine (Fig. 4b). The spiny glassy fragments are dark, spiny scoria that range in shape from subrounded to angular (Fig. 4c). These fragments contain abundant glassy areas, while the spiny opaque fragments lack a glassy, iridescent surface. Both groups of spiny clasts are characterized by the presence of dark and light brown glass. The spiny opaque fragments are the densest fragments and have the largest amount of crystals. They contain, as the most abundant phase, relatively large meso- and micro-crysts of plagioclase, up to 3 mm long, together with meso- and micro-crysts of clinopyroxene and

13

olivine (Figs. 4c and 4d). In the dark portions of their matrix, tiny fibrous microcrysts of olivine + clinopyroxene + plagioclase + Fe-Ti oxides occur. The spiny glassy fragments have the same crystal populations as the spiny opaque ones, but their plagioclases are much smaller and attain a maximum length of only 0.3 mm. Clusters of plagioclase and clinopyroxene are present in both the spiny opaque and the spiny glassy fragments, as well as rare macrocrysts of olivine. The olivine macrocrysts exhibit the typical compositional (Fo 84.2) and petrographic features of olivine phenocrysts described in previous studies (Clocchiatti et al., 1979; Albarede and Tamagnan, 1988; Bureau et al., 1998a and b; Famin et al., 2009; Welsch et al., 2013). They are automorphic, fractured with oxides (mostly chromite) and melt inclusions (Fig. 4c). Fluidal and pumice fragments studied for textures contain rare macrocrysts and mesocrysts of olivine, and the crystals are essentially microlites. The pumice and some fluidal fragments have lower contents of microlites than some fluidal and spiny fragments, with the latter having the highest microlite content (Table S4). For comparison two fragments of lava have been analyzed as well (Table S3). The lava fragments are poorly vesiculated and completely crystalline (Fig. 4e). The lava contains the same paragenesis of crystals described in the spiny opaque fragments, with the main difference that its matrix is completely crystallized and constituted mostly by well-formed plagioclase up to 800 microns and clinopyroxene up to 500 microns. Scarce, smaller olivines, are also present. Evidence of post emplacement crystallization is mainly constituted by the large amount of tiny rounded Fe-Ti oxides ubiquitous dispersed.

The componentry results are reported in Figure 5 for the Main Vent deposits; the deposits from the Fractures are characterized exclusively by fluidal clasts (Fig. 3). At the base of the Main Vent deposit, the coarse fraction of the deposit is rich in golden and fluidal components that represent more than 60-70 vol% (Figs. 5a and 5b). The proportion of the two groups is similar. If we look at the Morphologi G3 results (Fig. 5c) for the coarse ash fragments, this population is formed exclusively by smooth fragments that correspond to fluidal and golden pumice. In contrast, in the upper, coarse grained fall deposit, the clasts bigger than 8 mm are dominated by the spiny scoria fragments, while the fraction smaller than 8 mm show a dramatic increase in the golden and fluidal fragments, with the fluidal ones always more abundant than the golden ones (Figs. 5a and 5b). The small amount of coarse ash fraction in the top deposit, however, is dominated by the presence of spiny fragments (Fig. 5c). Abundant light, golden, coarse lapilli pumice and bombs have been found scattered laterally up to 30 metres from the main axis and were not found in the proximal deposit. On the basis of the high amount of pumice in the lower part of the deposit, we correlate the large,

14

461   light clasts with the base of the proximal deposit, and consequently we interpret them as

462   material emitted at the beginning of the June 2014 eruptive event.

463

464   **4.2 Particle density, porosity connectivity permeability and texture**

465   Density analyses performed on 200 coarse lapilli reveal a large variation in density values

466   from 390 kg/m^{-3} to 1700 kg/m^{-3} with a median value at 870 kg/m^{-3} (Table S3). The fragments

467   collected from the Main Vent have a bimodal density distribution, with a main population of

468   light fragments having a mode at 800 kg/m^{-3}, and a second and denser population centered at

469   1400 kg/m^{-3} (Fig. 6a). The golden and fluidal fragments form the lower-density population

470   and the spiny fragments are dominant in the denser population (Fig. 6a). For these samples

471   there is a marked correlation between porosity and morphology, so that the spiny-opaque

472   clasts are the densest (up to 1600 kg m^{-3}, with a vesicularity of 45 vol%) and the golden

473   pumice are the lightest (minimum density of 390 kg m^{-3} with a vesicularity of up to 86 vol%;

474   with a Dense Rock Equivalent density of 2.88 x 10^3 kg m^{-3}). ~~bimodal distribution, with a main~~

475   ~~population of light fragments having a mode at 800 kg/m^{-3}, and a second and denser~~

476   ~~population centered at 1400 kg/m^{-3} (Fig. 6a).~~ The fluidal fragments~~, mostly~~ collected at the

477   Western Fracture (Fig. 1b~~a~~), have a density range from 7~~6~~00 to 1400 kg/m^{-3} and a mode at

478   1000 kg/m^{-3} (Fig. 6b). The five fragments from the only bomb collected at the Upper Fracture

479   are characterized by two distinct density values, the low density one (700-800 kg/m^{-3}) refers

480   to the core of the sample, while the high density one (1400-1500 kg/m^{-3}) represents the

481   quenched external rim of the bomb. ~~The bulk deposit collected close to the Main Vent has a~~

482   ~~bimodal density distribution, with the golden and fluidal fragments forming the lower density~~

483   ~~population and the spiny fragments being dominant in the denser population (Fig. 6). For~~

484   ~~these samples there is a marked correlation between porosity and morphology, so that the~~

485   ~~spiny-opaque clasts are the densest (up to 1600 kg m^{-3}, with a vesicularity of 45 vol%) and the~~

486   ~~golden pumice are the lightest (minimum density of kg m^{-3} with a vesicularity of up to 86~~

487   ~~vol%; with a Dense Rock Equivalent density of 2.88 x 10^3 kg m^{-3}).~~ Finally, the two fragments

488   of lava show the ~~lowest~~~~highes~~highest density values at 1800 and 2150 kg m^{-3}. This last value

489   is one of the ~~lowest~~highest found in the lava collected from 2014 up to 2017 (see Fig. 13 in

490   Harris et al., 2017 and unpublished data)

491   In all these samples, t~~T~~he increase in vesicularity correlates with an increase in the

492   amount of small (0.1 mm), medium (0.5-1 mm) and large (up to 4 mm) vesicles. In the fluidal

493   clasts, these vesicles have a regular rounded or elliptical shape and are scattered throughout

15

the sample. The lightest pumices are often characterized by the presence of a single, large central vesicle (10 – 15 mm) with the little vesicles and a few medium vesicles distributed all around it (Fig. 4). The spiny glass texture is characterized by a lower amount of large vesicles than in the pumice and by the presence of mostly medium sized vesicles, while the spiny opaque has more irregular shaped, very large (up to 10 mm) vesicles with a small and a medium sized bubble population. In the spiny glass samples, the glass is more or less brown, with the dark brown portions being the ones with the lowest vesicle content and the highest microlite content. The opaque samples have a central, very dark glass portion, with low vesicle content, and a more vesicular glassy portion at the outer edges (Fig. 4). The two fragments of lava are poorly vesiculated (Fig. 6a) and characterized by large, irregular vesicles (up to 5 mm in diameter). Cluster of small vesicicle (up to 0.1 mm) are scattered between the large ones.

The VSD histograms picture well the decrease in percentage of vesicles from the golden to the lava (Fig. 4) as well as the increase in coalescence and or expansion in the spiny fragments, marked by the increasing of the large vesicles population (Figs 4c and 4d). This trend is also marked by the decrease in number of vesicle for unit of volume (N_v, Fig. 4) from the golden to the lava. Finally, the trend is also mirrored by the total percentage of crystals (calculated in 3D, Fig. 4 and reported both in 3D and 2D for each sample in in Table S3) that increases with the increase of density of the clasts, from a minimum of 8% in vol. for the golden up to 55 % in vol. for the spiny opaque scoria, up to 100 % in vol. for the lava (Fig. 4). Mesocrystals, formed mostly by the same proportion of plagioclase and clinopyroxenes are absent or very scarce in the golden and fluidal fragments, while they reach their maximum values, up 21% in vol. in the spiny opaque fragment. The ~~microcrystals~~ population of microcrystals is mostly constituted by plagioclases that range from a minimum of 6 % in vol. in the golden, up to 23-25 % in vol. in the spiny fragments and to 64 % in vol. in the lava.

The connectivity data (Fig. 6c~~d~~) also indicate that the fluidal and golden clasts have a larger amount of isolated vesicles (up to 40% in volume) ~~in~~with respect to the spiny products. The fluidal clasts from the Western Fracture are the most homogeneous with an average percentage of isolated vesicles around 30% in volume. In contrast, b~~B~~oth the pumice and the fluidal fragments from the Main Vent, characterized by higher values of porosity (> 75%), have a wide range in~~er~~ percentage of isolated vesicles (between 20 and a few percentage in volume)~~with high vesicularity are characterized by fewer amounts of isolated vesicles~~. The fragments of the bomb collected at Upper Fracture are consistent with a vesiculated core characterized by scarce isolated vesicles and the quenched rind that has 30 % of isolated

16

528 vesicles. Finally the spiny fragments have the lowest content of isolated vesicles (0-5% in
529 volume). Although the presence of these isolated vesicles, all the samples shear high values of
530 permeability (Fig. 6d).

4.3 Chemistry and geochemistry of the products

533 Major and trace element concentrations of whole-rock and hand-picked glass samples are
534 reported in Table S4. Whole rock major element composition is very uniform (e.g.,
535 6.5<MgO<6.7 wt%) and well within the range of Steady State Basalts (SSB), the most
536 common type of basalts erupted at Piton de la Fournaise (Albarède et al., 1997). However,
537 compatible trace elements, such as Ni and Cr, are at the lower end of the concentration range
538 for SSB (<100ppm) indicating that the June 2014 eruption sampled relatively evolved melts.
539 Ni and Cr generally show higher concentrations in 2014 bulk rocks (79<Ni<92ppm and
540 71<Cr <87ppm) compared to the 2014 glass chips (66<Ni<73ppm and 54<Cr <59ppm for all
541 but two chips). In the Cr vs Ni plot (Fig. 7a), whole rocks plot to the right of the main
542 clinopyroxene +/- plagioclase–controlled melt differentiation trend. This trend is controlled by
543 the addition of Ni-rich olivine (Albarède and Tamagnan, 1988). We estimate that the Ni
544 excess results from the occurrence of a low amount (0.7 to 1.3 wt%) of cumulative olivine in
545 whole rocks, consistent with thin section observations. The composition of olivine
546 macrocrysts (ca. Fo84) is too magnesian to be in equilibrium with the low-MgO evolved
547 composition of the 2014 magma. Using our estimate for the amount of cumulative olivine, we
548 recalculate the olivine–corrected MgO content of the 2014 magma at 6.2 wt%. The June 2014
549 melt is thus only moderately depleted in compatible elements compared to the previous
550 eruption of December 2010 (MgO~6.6 wt%, Ni~80 ppm, Cr~120 ppm). Conversely, the June
551 2014 melt is significantly depleted in compatible elements compared to the earlier November
552 2009 eruption, which sampled relatively primitive magmas (average MgO~7.7 wt%, Ni~135
553 ppm, Cr~350 ppm) (Fig. 7a). The 2014 evolved composition plots at the low-Ni-Cr end of
554 Piton de la Fournaise historical differentiation trend (Albarède and Tamagnan, 1988), near the
555 composition of lavas erupted on 9 March 1998 after 5.5 years of quiescence (1992-1998).
556 Note that olivine accumulation at PdF generally occurs in melt having ca.100 ppm Ni
557 (Albarède and Tamagnan, 1988). Olivine accumulation in evolved melts (Ni < 70 ppm) seems
558 to be a distinctive feature of many small post-2007 eruptions (e.g. this event and the three
559 2008 eruptions, see Di Muro et al., 2015).

17

560   A closer inspection of Ni-Cr variability in June 2014 whole rock samples (Fig. 7b)
561   reveals that scoria from the Western Fracture (140624-9b-6, Table S4) and early erupted lavas
562   (1406-21-1, Table S4) have the lowest amount of olivine (<0.9%) whereas scoria from the
563   Upper Fracture (140624-13a) and late erupted lavas (140324-12) have a slightly higher
564   amount of olivine (>1.2%). This is consistent with the general trends observed at PdF of
565   olivine increase from the start to end of an eruption (Peltier et al., 2009).

566   The so called "olivine control trend" in Ni-Cr space cannot be explained either by
567   addition of pure olivine (which contains less than 500 ppm Cr (Salaün et al., 2010; Di Muro et
568   al., 2015; Welsch et al., 2009), or by the addition of olivine plus pyroxene (which would
569   require ca. 50% pyroxene with 970 ppm Ni and 4800 ppm Cr, see Fig. 7 caption). Instead,
570   addition of olivine hosting ca. 1% Cr-spinel (with 25 wt.% Cr) accounts for data and
571   observations, and is consistent with crystallization of olivine and Cr-spinel in cotectic
572   proportions (Roeder et al., 2006). The fact that some samples (golden pumice) plot off the
573   main, well-defined array, can be explained either by addition of more or less evolved olivine
574   crystals (with the range of Fo 80-85 measured in June 2014 samples) and/or slight variations
575   ($\pm$ 0.02%) in the proportion of Cr-spinels (Fig. 7b).

576   The glass chemistry of the four clast types allows us to correlate porosity and oxide
577   contents and shows an increase in MgO from the spiny opaque to fluidal and golden
578   fragments (Fig. 8a). Consistent with petrological and textural observations, the spiny opaque
579   is the most heterogeneous type of clast in terms of glass composition (Fig. 8). The glassy
580   portion at the edge of the clast is similar to the spiny glass, while the interior, characterized by
581   dark areas rich in tiny fibrous microcrysts, shows scattered glass compositions with very low
582   MgO content as well as a decrease in CaO (Fig. 8). We attribute the significant variation in
583   glass composition within the different components to variable degrees of micro-crystallisation
584   as the bulk chemistry of all clasts is very similar and globally homogeneous.

585

586   **4.4 Melt inclusions**

587   MI analyses must be corrected for post-entrapment host crystallisation at the MI - crystal
588   interface. We used a $Kd = (FeO/MgO)_{ol} / (FeO/MgO)_{melt} = 0.306$ (Fisk et al., 1988; Brugier,
589   2016) and an average $Fe^{3+}/\Sigma Fe_{total}$ ratio of 0.11 (Bureau et al., 1998a; Di Muro et al., 2016 and
590   references therein) defined for PdF magmas. For the June 2014 melt inclusions, the post
591   entrapment crystallization (PEC) ranges from 2.9 to 10.5 wt%. Raw and corrected major and
592   volatile element concentrations of MIs are reported in Table S6.

18

593   Host olivines span a large compositional range from Fo_{80} to Fo_{86}. Despite the evolved

594   bulk composition of the magma, most olivines are quite magnesian (Fo_{83-85}) and are not in

595   equilibrium with the evolved host magma. On the contrary, Mg-poor olivines (Fo_{80-81}) can be

596   considered as being in equilibrium with the bulk rock composition. The corrected

597   compositions of MIs in phenocrysts from the different samples partly overlap with the

598   evolved bulk rocks (MgO_{wr}: 6.1-7.2 wt%) and extend to higher MgO contents of up to 8.8

599   wt% (Table S6). MIs display a narrow range of transitional basaltic compositions (K_2O= 0.5-

600   0.9 wt%) and show no significant difference between the three types of scoriae. The major

601   element composition of melt inclusions correlates with that of the host olivines. Melt

602   inclusions in the high Fo-olivines have the highest MgO, CaO and TiO_2 and lowest K_2O

603   concentrations (Table S6). It is interesting to note that the June 2014 products contain two

604   populations of magnesian ($Fo_{>83}$) olivines hosting melt inclusions with two distinct Ca

605   contents. Most of the magnesian olivines contain MIs with unusually high CaO contents (11.6

606   – 12.9 wt%) and high CaO/Al_2O_3 ratios (0.8-0.9), higher than that of the bulk rocks (0.8) (Fig

607   8). The occurrence of olivines with "high Ca" melt inclusions has been observed in all three

608   different types of scoriae. A few magnesian olivines and all Mg-poor olivines ($Fo_{80.5-83.6}$) host

609   MIs with lower CaO contents (11.4 wt%). This latter composition overlaps with that of the

610   bulk rock (Fig 8). The "high Ca" population of inclusions is also enriched in TiO_2 and Al_2O_3

611   and depleted in MgO, FeO_T and Na_2O for a given olivine Fo content with respect to the "low

612   Ca" population. Both low- and high-Ca populations of melt inclusions have similar K_2O

613   contents and total alkali content increases from 3 wt% at 12.6 wt% CaO, to 3.5 wt% at 10.8

614   wt% CaO. However, we remark that high Ca melt inclusions from the June 2014 activity

615   record a significant scattering in K_2O contents, which range from 0.55 to 0.9 wt%. These

616   anomalous compositions potentially track processes of crystal dissolution (e.g. pyroxene

617   dissolution).

618   MIs in olivines from June 2014 can best be compared with those of other recent small-

619   volume and short-lived eruptions which emitted basalts with low phenocryst contents, like

620   those in March 2007 (0.6 Mm^3) and November 2009 (0.1 Mm^3) (Roult et al., 2012). March

621   2007 aphyric basalt has a bulk homogeneous composition with intermediate MgO content

622   ($MgOwr$: 7.33 wt%; K_2O: 0.67 wt%). Their olivines (Fo 81) are in equilibrium with the bulk

623   rock and their composition is unimodal (Di Muro et al., 2014). November 2009 products are

624   the most magnesian lavas emitted in the 2008-2014 period, slightly zoned ($MgOwr$: 7.6-8.3

625   wt%; K_2O: 0.75 – 0.62 wt%) and contain a few percent of normally zoned olivine macrocrysts

626   with bimodal composition (Fo81 and Fo83.5, see Di Muro et al., 2016). June 2014 bulk rocks

19

627 (MgO_{wr}: 6.7 wt%; K_2O: 0.75 wt%) and melt inclusions in Fo_{80-81} olivines are quite evolved.

628 Their composition is close to that of products emitted by summit intracaldera eruptions in

629 2008, ca. 1.5 years after the large 2007 caldera forming eruption (Di Muro et al., 2015) (Fig.

630 8). As already reported for 2008 products, many olivine macrocrysts of 2014 are clearly too

631 magnesian to be in equilibrium with the relatively evolved host melts. Overall, MgO content

632 in 2007-2014 melt inclusions tends to decrease with decreasing Fo content of the host

633 olivines. MIs in olivines also exhibit a trend of linear decrease in MgO and increase in FeO

634 from April 2007 to 2009-2014 products (Fig. 9). Melt inclusions in March 2007, November

635 2009 and June 2014 follow the same trend of FeO enrichment (Fig. 9). In the large-volume

636 and olivine-rich April 2007 products, MIs in magnesian olivines with $Fo_{>82}$ have distinctly

637 higher MgO, FeO and lower SiO_2 and Al_2O_3 than MIs in 2009-2014 products. The distinctive

638 FeO enrichment of many of the MIs from the April 2007 oceanite has been interpreted by Di

639 Muro et al. (2014) as a result of post-entrapment modification ~~during long~~related to new

640 magma inputs into long lasting magma storage.

641   Two populations of low- and high-Ca melt inclusions are also found in the November

642 2009 olivines. Low-Ca melt inclusions from the November 2009 and June 2014 eruptions

643 indicate a single trend of chemical evolution (Fig. 8), consistent with bulk rock compositions.

644 June 2014 products have lower MgO and CaO contents than those from November 2009.

645 Significant scattering in K_2O content (0.6-0.9 wt%) is found in low-Ca inclusions from 2009,

646 as observed in high-Ca inclusions from the 2014 eruption, but they share similar K_2O

647 contents. In 2009 and 2014 products, K_2O content of melt inclusions is partly anti-correlated

648 with the olivine Fo content. This observation has been attributed to moderate heterogeneity of

649 primary melts feeding the plumbing system of PdF. Rapid temporal changes of K_2O content in

650 PdF basalts have been reported (Boivin and Bachelery, 2009).

651

652 **4.5 Mineral composition and glass – plagioclase equilibrium**

653 All 2014 scoriae (spiny, fluidal, golden) contain the same paragenesis of olivine,

654 clinopyroxene and plagioclase. The composition of minerals found in golden, fluidal and

655 spiny scoriae is indistinguishable.

656   In olivines, average MgO content decreases from macrocrysts ($Fo_{84.1}$) to mesocrysts

657 ($Fo_{79.6}$) to microlites. Olivine microlites (Table S5) are normally zoned. Their composition

658 ranges from $Fo_{78.0-75.3}$ in the cores to $Fo_{74.3-70..5}$ in the rims. Overall, olivines in 2014 products

659 span the full range of typical Fo contents of recent Piton de la Fournaise magmas (Boivin and

20

Bachèlery, 2009; Di Muro et al., 2014; 2015). Clinopyroxene composition (augites) ranges from $En_{53}Fs_{15}Wo_{32}$ to $En_{41}Fs_{14}Wo_{45}$. Their average composition ($En_{45}Fs_{14}Wo_{41}$) is consistent with that found in other recent evolved melts like those emitted by the 2008 eruptions (Di Muro et al., 2015) and more generally in recent Piton de la Fournaise products (Boivin and Bachèlery, 2009). Clinopyroxenes are unzoned, the composition of cores and rims is very similar and close to that found in microcrysts and mesocrysts. Plagioclase composition ranges from $An_{79.5}Ab_{19.9}Or_{0.6}$ to $An_{63.1}Ab_{35.7}Or_{1.2}$ with a bimodal distribution ($An_{76.5-79.5}$ and $An_{63.1-72.9}$. Fig. 10a). Similar bimodal distribution~~s~~ w~~ere~~as observed in ~~the evolved 2008~~many other products, ~~in particular from the November 2008 eruption~~at PdF (Di Muro et al., 2015). Mesocrysts ($An_{75.5}Ab_{23.8}Or_{0.7}$ on average) are more calcic with respect to microcrysts ($An_{65.7}Ab_{33.1}Or_{1.2}$ on average). Normal zoning is ~~commonly~~ found from plagioclase cores to rims (Fig. 10a). The composition and zonation of 2014 plagioclases clearly ~~, which~~ contrast~~s~~ with the complex and often reverse zoning patterns and intermediate composition of the ~~previously reported for the~~ 2008 PdF products that were attributed to pre-eruptive magma heating (Di Muro et al., 2015).

Plagioclase-melt equilibrium and melt composition in pyroclastic rocks and water-quenched lavas were used to estimate both temperature and water content dissolved within the melt (Fig. 10b and Table S5). Temperature estimates are based on the (dry) equation of Helz and Thornber (1987) ~~modified~~ recalibrated by Putirka (2008). Dissolved w~~W~~ater content was calculated from the plagioclase hygrometer of Lange et al. (2009) at 50 MPa. This pressure correspond~~sing~~ to the ~~maximum~~ average CO_2-H_2O saturation pressure ~~estimation~~ (recalculated with Papale et al., 2006)~~,~~ typically recorded in melt inclusions from central products at PdF (e.g. 1931 eruption in ~~; (~~Di Muro et al., (2016) and references therein). This pressure roughly corresponds to the sea level depth, which is inferred to be the location of the potential main shallow magmatic reservoir (Peltier et al., 2009; Lenglingé et al., 2016; Coppola et al., 2017). The application of the plagioclase hygrometer of Lange et al. (2009)~~hydrous thermometer of Putirka (2008)~~ makes it possible to estimate the dissolved water content in the melt with a nominal uncertainty of 0.15 wt% and is only slightly dependent on pressure. Plagioclase compositions not in equilibrium with the melt (glass or bulk rock) are those mesocryst cores with the highest ($An_{>76.5}$) anorthite content (Fig. 10a and Table S5). Such compositions are more in equilibrium with CaO-richer magnesian melts than those measured in matrix glasses and bulk rocks of 2014 eruption and likely formed during early stages of shallow magma differentiation (Fig. 10a).

In order to determine pre-eruptive conditions, calculations were performed only on paired plagioclase rims and matrix glasses in equilibrium, using the plagioclase-melt equilibrium constant of Putirka (2008) calibrated for melts whose temperature exceeds 1050°C (Kd_{An-Ab} = 0.27±0.05). Our review of published and unpublished data shows that melt temperature progressively decreases from April 2007 (1188+/-16 °C) to January-October 2010 (1147+/-9°C) and positively correlates with K_2O content in melts which increases from 0.70 to 0.96 wt% (Fig. 10b). The melts from the June 2014 eruption record the lowest temperatures in post-2007 eruptions (1131±15 °C) together with the highest K_2O-enrichment (K_2O: 0.90±0.12 wt%). The lowest temperatures are recorded by spiny scoriae, while the temperature of golden scoriae overlaps with that of 2010 products emitted before the 2010-2014 phase of quiescence. In spite of the large variability in melt composition and temperature, average pre-eruptive water content dissolved in the melts (0.5 +/- 0.2 wt%) is quite homogeneous for the whole 2008-2014 period. In 2014, the lowest estimated dissolved water content (down to 0.38 wt%) is for the golden and some fluidal scoriae, while the maximum amount (0.68 wt%) is for the spiny opaque scoriae. However, water content estimated from core-bulk rock equilibrium (0.3±0.1 wt%) is slightly lower than that estimated from rim and microlite-matrix glass equilibrium (0.5±0.2 wt%), but the difference broadly overlaps the nominal uncertainty related to calculations. Dissolved water contents in melts of the pyroclasts are thus ~~lower than~~intermediate between those measured in 2007 melt inclusions (H_2O: 0.8 +/- 0.15 wt% and up to 1.1 wt%) and ~~higher than~~those typically found in degass~~ing~~ed matrices of lava and Pele's hairs of 2007 (Fig. 10; 0.2 wt%; see Di Muro et al., 2015; 2016).

5 Discussions

5.1 ~~The activity~~Eruptive dynamics

The activit~~y~~ fed by the uppermost Western Fractures and Upper Fractures (Fig. 1) w~~as~~as very short-lived, as shown by the presence of only scattered bombs and coarse lapilli (Fig.~~s~~ ~~3c~~ 3d and 3~~c~~d). The homogeneity of these clasts, their coarse grained nature and the fluidal smooth texture are in agreement with very short-lived fire-fountaining/magma jets. Glassy outer surfaces of clasts have been interpreted as a late-stage product of fusion by hot gases streaming past the ejecta within the jet/fountain (Thordarson et al., 1996; Stovall et al., 2011). However, the occurrence of this process is not supported by the homogeneous glass composition in our fluidal clasts. Therefore, we interpret these features here just as rapid

quenching and not re-melting. Vlastélic et al. (2011) have documented the mobility of alkalis and other elements on PdF clasts having experiences long exposures to acid gases, that in the 2014 events is preventinged by the short duration of the events.

At lower altitude and close to the Main Vent (Fig. 1), the 5 cm layer at the base of the fall deposit is fine-grained (Figs. 3b and 3c), rich in fluidal and golden fragments (Fig; 5), with a perfect Gaussian grain size curve (Fig. 5), and similar to that reported from the weak 2010 fountaining event (Fig. 3e 3f and Hibert et al., 2015). Therefore, we interpret this deposit as being due to weak Hawaiian like fountaining (sustained, but short-lived) activity. We want to remark here that this activity happened during the night and was not observed. The top of the same deposit is coarse grained (Figs 3b and 3c), bimodal, has a lower content in coarse ash (Table S2) and is rich in spiny opaque and spiny glass fragments (Fig. 5). The reverse grain size likely records the transition from early continuous fountaining to late discrete Strombolian activity (observed and recorded the 21 of June 2014, Fig. 2). This transition in activity is typical of many eruptions at PdF (Figs. 2a and 2b and Hibert et al., 2015). The reverse grading of the whole deposit (Figs. 3b and 3c) is thus not correlated with an increase in energy of the event, but with two different eruptive dynamics and fragmentation processes. The decrease in coarse ash, which correlates with the decrease in energy of the event, highlights the most efficient fragmentation process within the Hawaiian fountaining with respect to the slow gas ascent and explosion of the Strombolian activity. These conclusions are consistent with (i) the continuous and progressive decrease in intensity of Real time Seismic Amplitude Measurement recorded by the OVPF seismic network (unpublished data), and (ii) satellite derived TADR (Coppola et al., 2017) which suggest continuous decay of magma output rate after an initial short-lived intense phase (Coppola et al., 2017).

5.2 Interpretation of the different textural signatures and the meaning of the 4 typologies of clasts.

1) Background on the texture of clasts from Hawaiian and Strombolian activities

The first microtextural analysis of Hawaiian ejecta was performed by Cashman and Mangan (1994) and Mangan and Cashman (1996) on pyroclasts from 1984 to 1986 Puʻu ʻŌʻō fountainings. The authors defined two clast types: 1) 'scoria' consisting of closed-cell foam of ≤85% vesicularity, with round, undeformed, broadly-sized vesicles, and 2) 'reticulite', an

23

open-cell polyhedral foam with ~1 μm thick vesicle walls with >95% vesicularity. They stated that the scoria to reticulite transition is a consequence of Ostwald ripening, where larger bubbles grow at the expense of smaller bubbles due to post-fragmentation expansion of clasts within the fountain. According to this model, scoria preserves textures closer to conditions at fragmentation, whereas continued vesiculation and clast expansion in the thermally-insulated core of the fountain results in reticulate. This model was confirmed at lava fountains at Etna (Polacci et al., 2006), Villarrica (Gurioli et al., 2008), Kīlauea Iki, (Stovall et al., 2011 and 2012), Mauna Ulu (Parcheta et al., 2013) and Al Madinah (Kawabata et al., 2015). These last authors also measured the connected and isolated porosity in the AD1256 Al-Madinah Hawaiian fountaining eruptions. They found that the reticulite-like textures from the central part of these very high fountains showed isolated vesicles in agreement with low shear rates and low viscosity melts, where bubbles may grow spherically and remain isolated. In contrast, at margins of the fountains, high shear may lead to stretching and mechanical coalescence of bubbles, forming the common, fluidal types of particles seen also in the deposits. They also stated that lower vesicularity and greater isolated porosity were found in some tephra interpreted as resulting from Violent Strombolian eruptive phases.

The data that we found in our study of the typical activity of PdF agree only partially with all these interpretations. The reason is that we sampled and measured products of very weak Hawaiian to Strombolian activities. If we plot the approximate durations and masses of these events on the Houghton et al. (2016) diagram, the 2014 activity of PdF falls into the two fields for transient and fountaining activity, but at the base of the diagram. We here show for the first time that short lived and weak fountaining can preserve pyroclast textures that can be considered as representing a valid approximation to magma ascent and fragmentation conditions before the explosions and also provide some information about the ~~shallow reservoir~~pre-eruptive storage conditions. The occurrence of time-variable ascent conditions is also reflected in the time evolution of ~~explosion~~eruptive dynamics, with the golden and fluidal emitted from the low fountaining episodes and the spiny fragments from the Strombolian-like explosions

2) The four typologies of clasts and their distribution in space and in time in the 2014 eruption at PdF

So, as described in 5.1, longitudinal variation in eruptive style along the fracture system produces a spatial variability in the proportions of the four typologies of clasts. The

uppermost fractures (Western and Upper Fractures, Fig. 1a) are characterized solely by fluidal fragments (Fig. 4b); they lack both the spiny and the golden components. In addition, these fluidal clasts are the ones showing the smoothest surfaces (indicative of rapid quenching in a very hot environment), low porosity values (between 50 to 77%, Fig. 6b), the highest content in isolated vesicles (~ 30% in vol. Fig. 4c), and low vesicle numbers (3 to 5 x 10^6, Fig. 4b), comparable to the spiny fragments. They have scarce mesocrysts (1-2 % in vol. Table S3) and very low amount of microcrysts of plagioclase and clinopyroxene (3 to 11 % in vol., Table S3). These fluidal scoria fragments were emitted by short lived jets of magma, therefore they underwent rapid quenching in a very hot environment that prevented any expansion or further vesiculation and preserved a very high number of isolated vesicles (Fig. 6d). Syn-eruptive crystallization was hindered by high ascent velocities in the dyke, due to the sudden release of over-pressure in the shallow magma reservoir.

The four typology of clasts, golden pumice, fluidal scoria and the spiny fragments (Fig. 4), were found associated only at the Main Vent. The proportion of these fragments correlate with the eruptive dynamics, being the golden lapilli and fluidal clasts dominant in the Hawaiian, more energetic activity at the beginning of the eruption (during the night between the 20 and the 21 of June 2014) and the spiny fragments dominant during the Strombolian activity, coinciding with the decreasing in Mass Discharge Rate (MDR, early in the morning of the 21, Fig. 2 and Coppola et al., 2017). The golden and fluidal fragments from the Main Vent show the highest porosity (86 %, Fig. 6a) variable proportions of isolated vesicles (Fig. 6c) and high, but variable, N_V numbers (Figs. 4a). They are also characterized by a uniform vesicle size population with clear evidence of incipient expansion, especially in the fluidal fragments (Figs. 4a and 4b). From the connectivity graph, there is a clear decrease in isolated vesicles with the increase in vesicularity (Fig. 6c). The content in crystal, mostly formed by microcrysts of sodic plagioclase (Fig. 10a) due to magma degassing during its ascent and decompression in the conduit (Di Muro et al., 2015), is very low, especially in the golden pumice (up to 15% in vol.), and slightly higher for the fluidal clasts (up to 23 % in vol.). We interpret the golden fragments, at the Main Vent, to be the fastest (low amount of microcrysts) and less degassed magma (high vesicularity coupled with high N_V), which experienced only a very short residence time in the magma transport system (dyke+vent), followed by the fluidal fragments. In contrast the spiny fragments, characterized by higher percentage of microcrysts and mesocrysts, by the lack of isolated vesicles, by the presence of coalescence signature and low N_V values (Figs. 4c and 4d), are indicative of an extensively degassed and cooled magma. The

25

presence of the mesocrysts (that formed in the shallow reservoir) in the spiny fragments, and their slightly cooler temperature (Fig. 10b), strongly support this interpretation. The spiny fragments likely record the slowest ascent velocity and the longest residence time in the reservoir+dyke+vent system compared to the golden/fluidal counterpart. Therefore these fragments are associated with Strombolian events, and decreasing in MDR of the activity, in agreement with their slower ascent that allow large syneruptive crystallization.

Among spiny fragments, the opaque ones are the densest, they lack a uniform glassy surface, and they are characterized by i) very high microlite content, ii) strong coalescence signature (Fig. 4d), iii) heterogeneous glass chemistry, and iv) mingling with hotter magma at the clast edges (Fig. 8a). All these features reveal the composite nature of these clasts. We interpret the spiny opaque as spiny glass fragments recycled inside the eruptive vent during the explosions, being the densest portion of the magma prone to fall back in the vent/fracture (Fig. 2b).

3) Degassing-driven versus cooling-driven crystallization

Syn-eruptive degassing is favoured by bubble connectivity/permeability in the ascending magma, enhanced by syn-eruptive crystallisation in the conduit (especially microcrysts of plg, Fig. 10a), even for magmas at low vesicularity. However, our dataset also support the occurrence of magma stratification in the reservoir. Textural and petrological data demonstrate that the initial activity emitted a small volume of melt (represented by golden and large part of the fluidal fragments) with very scarce crystals. This crystal-poor melt was followed in time by the main volume of magma that contains a larger amount of mesocrysts (spiny clastst and lava). Lava flows represent the main volume emitted in the 2014 eruption. Mesocrysts are absent in the golden, scarce in the fluidal and more abundant in the spiny (Figs 4b c and 4d) and lava (Fig. 4e) and consist in an equal percentage of plg and cpx and minor olivine. Their composition indicate that they formed in the reservoir, as shown by their different composition in respect to the microcrysts counterparts (Fig. 10a) that formed during melt degassing in the conduit. Most important, a large amount of microcrysts in lava formed in the reservoir as well during magma cooling (Figure 10a). So, we have a range of crystallization conditions. The fact that the lighter plg are not concentrated in the upper and early erupted portion of the reservoir can be due either to the fact that often they are locked in clusters with the cpx or that this melt was expelled from the crystal-rich portion of the reservoir (see Figure 10b). Water exsolution from the melt can result from its extensive crystallization, which

26

induces an increase in dissolved volatile content, up to saturation (second boiling) and can drive melt-crystal separation.

In conclusion, the crystals in the 2014 fragments do reflect the shallow reservoir conditions and the ascent degassing processes. Can we affirm that the vesicularity provide similar informations?

4) Textural syn-eruptive versus post fragmentation modifications

To prove that the 2014 clasts have been not modified by post fragmentation expansion process, following Stovall et al. (2011), we use a plot of vesicle-to-melt ratio (V_G/V_L, after Gardner et al., 1996) and vesicle number density (N_V, Fig. 11). As ~~explained~~demonstrated by Stovall et al. (2011), addition of small bubbles leads to an increase in N_V and only a slight increase in V_G/V_L. Bubble growth by some combination of diffusion and decompression leads to an increase in V_G/V_L at constant N_V. N_V decreases while V_G/V_L increases during bubble coalescence, whereas loss of bubbles via collapse or buoyant rise leads to a reduction in both parameters. Intermediate trends on the diagram reflect combinations of more than one of these processes. The pumice and the scoria from the Main Vent of PdF show the highest V_G/V_L, but also the highest Nv, suggesting preservation of small vesicles and growth by some combination of diffusion and decompression. The presence of the small vesicles confirms that the weak PdF activity leads to only limited post-fragmentation expansion inside the hot portions of the short-lived fountains. These data contrast with the data from the more energetic fountaining events observed at Kilauea or elsewhere, where pre-eruptive information is basically erased because pumice textures are dominated by expansion effects due to their longer permanence within the long-lived energetic fountaining. In contrast, the densest, spiny scoriae and the scoria from the Fractures activity show the lowest values of Nv and V_G/V_L, due to incipient coalescence and/or loose/lack of small bubbles.

According to previous works (listed above), the golden pumice of PdF should be derived from the central part of the fountains, but they do not show the strong post expansion signatures reported in the literature (Fig. 11). It is interesting to note that the fluidal fragments at the Main Vent are less smooth (Fig. 4), more vesiculated, and have a lower content of isolated vesicles than the fluidal scoria from the uppermost Fractures (Fig. 6). Therefore fluidal fragments at the 2014 Main Vent could indeed represent clasts that have been partly modified during their residence in the external part of the fountains, while the golden samples could come from the central part (Stovall et al., 2011 and 2012). However, the slight

differences in crystallinity and glass chemistry between the fluidal and golden fragments support the idea that each of these fragments has an imprint from the pre-fragmentation setting. In contrast, the spiny fragments from the Main Vent and the fluidal fragments from the Fractures show low N_V and low V_G/V_L in agreement with loss of vesicles and coalescence. However, the presence of large numbers of isolated vesicles within the fluidal scoria from the Fractures agrees with their provenance from a fast hot ejection of relatively degassed magma (low N_V). In contrast the spiny fragments, especially because of the presence of abundant mesocrysts and increase in syneruptive microcrysts, are indicative of the slowest ascent velocity and extensively degassing and cooled magma. The spiny fragments are the most degassed, densest and the most crystal rich magma that was emitted during low-energy activity by Strombolian explosion, where recycling phenomena were also very frequent (Fig. 2f).

Our findings are in full agreement with the recent review of Colombier et al. (2017b). According to these authors, connectivity values can be used as a useful tool to discriminate between the basaltic scoria from Hawaiian (fire fountaining) and Strombolian activity. The broad range in connectivity for pumice and scoria from fire fountaining is interpreted simply as being due to variations in the time available before quenching due to differences in location and residence time inside the fountain. The fluidal fragments from the Western Fractures are the richest in isolated vesicles because they are transported by very short lived hot lava jets. In contrast, the higher connectivity observed in scoria from Strombolian activity is probably related to their higher average crystallinity, and more extensive degassing prior to the eruption, (Colombier et al., 2017b). The spiny surface of these Strombolian fragments is due to the fact that these weak explosions emit only a small solid mass fraction and the partially quenched dense clasts land quickly after a short cooling path through the surrounding atmosphere (e.g. Bombrun et al., 2015).

All the clast, from golden to spiny, are very permeable, independent on their vesicularity, crystal content and/or of the presence of isolated vesicles. This is in agreement with our interpretation that magma degasses during its ascent in the conduit and that promotes microlite nucleation (see the sodic plagioclase, Fig. 10a) before magma fragmentation (see also Di Muro et al. 2015 with the Pele's hairs ad tears samples for the three 2008 eruptions). Moreover, we always find that some of the spiny clasts (especially the opaque ones) are slightly less permeable that the golden and fluidal ones, but not as impermeable as we would expect by their low vesicularity.

In conclusion, we can state that i) the crystals lower the percolation threshold and stabilize permeable pathways and ii) this is true for the syn-eruptive sodic plagioclase that favor an efficient degassing in the relatively crystal-rich magma, because of their low wet angles that favor degassing against nucleation (Shea, 2017) and their aspect ratio (e.g. Spina et al. 2016) iii) therefore permeability develops during vesiculation through bubble coalescence, which allows efficient volatile transport through connected pathways and relieves overpressure (Lindoo et al., 2017). Pervasive crystal networks also deform bubbles and therefore enhance outgassing (Oppenheimer et al., 2015). Based on Saar et al. (2001) crystals should start to affect the behavior of the exsolved volatile phase when they approach 20 vol% (Lindoo et al., 2017). In our dataset, apart from the golden and part of fluidal, all the other clasts do have microlites >20%. Our data completely ~~agree~~support that slow decompression rate allows more time for degassing-induced crystallization, which lowers the vesicularity threshold at which bubbles start to connect.

Rapid re-annealing of pore throats between connected bubbles can happen due to short melt relaxation times (Lindoo et al; 2016). This phenomenology ~~can~~could explain the high amount of isolated vesicles in the fountaining samples. However, ~~if you look at the~~ vesicle distributions of the golden and fluidal fragments ~~, they~~ are almost perfect Gaussian curves, so it seems that if the relaxation process happens it just merged perfectly with the expected vesicle distribution. In contrast, coalescence and/or expansion (as we observe in the spiny fragments) do not fit the curves (Fig. 4). In addition, we should expect that in crystal-poor fragments, due to melt ~~ing~~relaxing~~s~~ and pathways closure, the clasts became impermeable after quenching, as revealed by some petrological experiments performed on crystal-poor basaltic magma (Lindoo et al., 2016). In contrast, in high crystalline magmas, the presence of micro-crystals increase~~s~~ viscosity thus preserving the coalesced textures (see Moitra et al., 2013). The isolated vesicle-rich fragments of the 2014 PdF eruption are highly permeable, and are characterized by variable range~~s~~ of porosity and numbers of vesicles (Fig.4 and Fig. 6d) that seem more related to the pre-eruptive conditions than to the post relaxation ~~phenomenon~~ of low ~~viscosity~~us ~~magma~~selts. In the 2014 crystal-poor samples, the permeability increases rapidly once the percolation threshold has been reached, and efficient degassing prevents bubble volumes from expanding past the percolation threshold (Rust and Cashman 2011). ~~-~~
~~*Degassing-driven-driven*sour datasetoccurrenceTextural and petrological data demonstrate that the initial activity emittedvery -was(spiny clastst; lava). Lava flows representemitted in the 2014 eruptionMicrophenocrysts areand . Their composition indicate thatedduring melt degassing Most important,during magma cooling and early eruptedof the reservoir either or~~

29

that this melt was expelled from the crystal-rich portion of the reservoir Water exsolution from the melt can result from its extensive crystallization, which induces an increase in dissolved volatile content, up to saturation (second boiling) and can drive melt-crystal separation.

5.4 Integration between the physical and textural characteristics of the products and their geochemical signature: insight into the feeding system

According to Peltier et al. (2016), the June 2014 eruption emitted magma from a shallow pressurized source located only 1.4-1.7 km below the volcano summit. Coppola et al. (2017) suggest that the 2014 event was fed by a single shallow and small volume magma pocket stored in the uppermost part of the PdF central plumbing system. All 2014 clasts show homogeneous and evolved bulk compositions, irrespective of their textural features. June 2014 products are among the most evolved products erupted since at least 1998 and are moderately evolved with respect to those emitted in 2010, just before the 2010-2014 quiescence. Bulk rock and melt inclusion data suggest that the 2014 evolved magma can be produced by crystal fractionation during the long lasting (4.6 years) storage and cooling of the magma injected and partly erupted in November 2009. The different types of scoria and pumice emitted in 2014 show significant variations in glass composition (Fig. 8b) due to variable degrees of micro-crystallization. In theory, microlites microcrysts and microphenocrysts can reflect late stage (during magma ascent and post-fragmentation) crystallization. In this case, their variable amount within, for instance, the glassy and opaque parts of the spiny scoria might reflect slower ascent velocity or longer residence time in the system (e.g. Hammer et al., 1999, Stovall et al., 2012; Gurioli et al., 2014) in agreement also with the vesicle signature. However, the four typologies of clasts differ also in terms of mesocryst content (from rare to 5 vol% for the golden and fluidal and 14-23 vol% for the glassy spiny and spiny opaque, respectively). Equilibrium plagioclase-melt pairs record an almost constant and moderate dissolved water content, intermediate between that expected for melts sitting in the main shallow reservoir (located close to sea level) and the degassed matrix of lavas. Dissolved water contents are thus consistent with pre-eruptive magma water degassing during its storage at shallow level, as suggested by geophysical data, and suggest that the plagioclase mesocrysts and some of the microlites in the spiny scoria and in the lava grew during magma storage. Melt composition records a potential pre-eruptive thermal gradient of ~30 °C between the hotter (pumice and fluidal) and the cooler (spiny) magma.

30

Tait et al. (1989) suggest that magma evolution can lead to oversaturation of volatile species within a shallow reservoir and trigger a volcanic eruption. At PdF, the golden and the fluidal clasts might represent the portion of magma ~~sitting in the~~located at the top of the shallow reservoir and ~~accumulating~~ enriched in bubbles of water rich fluids, released by the cooler, more crystallized and more degassed "spiny-lava" magma (Fig. 10b). The small volume of magma, its constant bulk composition and the very small inflation recorded prior to the eruption (Fig. 1d) could be consistent with an internal source of over-pressure related to volatile exsolution. Larger inflation rates over a broader area are expected when shallow reservoir pressurization is related to a new magma input from a deeper source. Slight baseline extensions both on distal and proximal sites suggest that magma transfer towards shallower crustal levels started short before (11 days) the final magma eruption. Geochemical data do not support the occurrence of a new magma input in the degassed and cooled 2014 reservoir. We can thus speculate that stress field change related to progressive deep magma transfer has promoted volatile exsolution, melt-crystal separation and melt expansion in the shallow reservoir. Textural heterogeneity of the 2014 products partly reflects a pre-eruptive ~~thermal~~ physical gradient recorded by the variability in crystal and bubble contents in the shallow reservoir feeding this eruption. The golden and fluidal fragments are the bubble richer and hotter portion of the melt. The spiny fragments are the degassed and cooler portion of the reservoir, whose progressive tapping led to a decrease in explosive intensity (from fountaining to Strombolian activity). Our results are also consistent with processes of mechanical reservoirs/dyke stratification, as ~~already~~ observed ~~experimentally~~ by Menand and Phillips (2007). ~~The golden and fluidal fragments are the bubble richer and hotter portion of the melt. The spiny fragments are the degassed and cooler portion of the reservoir, whose progressive tapping led to a decrease in explosive intensity (from fountaining to Strombolian activity).~~ As explained earlier, ~~this process is~~magma ascent promoted ~~enhanced by~~ syneruptive degassing induced crystallization. The spiny opaque clasts can be considered as being recycled material that fell back into the system. Accumulation of olivine crystals out of equilibrium with the host magma produces minor variations in mesophenocryst contents as observed within the same type of clasts sampled at different times/locations during the eruption, with the scoria from the Western Fracture and early erupted lava being the ones with the lowest amount of olivine (Table S4 and Fig. 7b). Again, this temporal variation supports an ~~slight~~ increase in large heavy crystals within the most degassed magma emitted toward the end of activity, ~~as observed as a general trend at PdF (Peltier et al., 2009)~~further suggesting that it correspond to the lower part of the reservoir.

1028

1029

Our dataset permits us to propose that the 2014 eruption was fed by a physically zoned magma reservoir with the lighter crystal-poor bubble-rich magma erupted first (and possibly located in the upper part of the storage system) that ascends faster and feed the more energetic phase, the fountaining. This lighter magma is not more evolved than the spiny one (same bulk compositions) and it is not necessarily richer in dissolved volatile amounts; it is just poorer in crystal and richer in bubbles. We conclude that the sSecond boiling, possibly triggered a few days before the eruption by stress field change, is responsible of the extraction of bubble rich melt from a crystal-rich network. This last one will represent the main volume of erupted lava. Fast ascent of the foam hinders its crystallization and preserve high number of vesicles, high vesicularity and it is only little modified by post-fragmentation expansion. Decrease in initial overpressure translates in a progressive decrease in magma ascent rate and output rate (e.g. Coppola et al., 2017 and references therein). Nucleation of microcrysts is enhanced in melt ascending with lower speed and is mostly related to syneruptive degassing (for the spiny).

The larger volume (dense lava) corresponds to crystallized and less vesiculated magma which experiences a slow ascent in the dyke and even further micro-crystallisation during its subaerial emplacement.

Melt inclusion results allow us to confirm the involvement of a single and only slightly heterogeneous magma source in 2014, related to cooling and fractional crystallisation of an older magma batch (November 2009). Interestingly, this latter short lived summit eruption was also characterized by the same large range of pyroclastic products found in 2014 in spite of its mafic composition.

This suggests that bubble accumulation and source pressurisation is highly dependent on the shallow storage depth, which facilitates rapid water exsolution (Di Muro et al., 2016), and it is not necessarily the outcome of slow magma cooling and differentiation (Tait et al., 1989).

6. Proposed model for the 2014 eruption and c~~C~~onclusions

In this paper we show that ~~a combination of~~ textural and petro-chemical ~~quantification~~ study of the eruptive products can be used to characterize the on-going activity at PdF and to ~~provide valuable information to understand both the~~constrain both the ~~causes~~trigger and the ~~dynamics~~ evolution of ~~these very~~ short-lived and small-volume eruptions. This approach resulted extremely valuable in i) understanding processes that lead~~ing~~ to an eruption which was preceded by short-lived and elusive precursors, ~~and ii) in~~to reconstructing the time evolution of eruptive dynamics in an ~~, when the geophysical precurs alone are not so strong and/or immediately dectetable and when the~~ eruption ~~is~~ with poor direct ~~not visually documented~~observation.

~~The June 2014 summit eruption occurred after a relatively long phase of quiescence (4.6 years) and was preceded by only a few days of weak and short geophysical seismic, geodetic and geochemical precursors (Peltier et al., 2016 and Fig. 1d). This multidisciplinary approach provides new constraints on the mechanisms triggering such short-lived, small but potentially hazardous eruptions~~ (STIAMO RIPETENDO TRE VOLTE GLI STESSI CONCETTI. RIASSUMI E TAGLIA). Following the sketch in Figure 12, we ~~suppose~~infer that residual magma from the 2009 eruption ~~was sitting~~ponding at shallow levels experienced long-lasting ~~colling~~cooling and crystallization (Fig. 12a). ~~During the inflation period (b~~Between 2010 and 2014 the volcano progressively deflated ~~,~~(Fig. 12b) possibly because of magma degassing and cooling, facilitated by the shallow depth of the reservoir. ~~itself allows exsolution, and magma with crystallization in situ of the~~During this phase mesocrysts and some micro~~lites~~crysts formed ~~, as observed in the lava sample~~ (Figs. 4e and ~~Fig.~~ 10a). ~~This process favours a physical zonation of the shallow reservoir. Therefore, magma storage at shallow depth favours volatile (mostly H₂O) exsolution at several steps during magma ponding, cooling and evolution (Fig. 12b)~~

The occurrence of deep (>10 km bsl) lateral magma transfer since March-April 2014 has been inferred by Boudoire et al., (2017) on the basis of deep (mantle level) seismic swarms and increase in soil CO2 emissions on the distal western volcano flank. The incipit of magma transfer towards shallower crustal levels is potentially recorded by subtle volcano inflation about 11 days before the June 2014 eruptions (Figs. 1d and 12c). We suspect that these deep processes can have progressively modified the shallow~~er~~ crustal stress field and ~~favored~~favoured magma vesiculation and~~,~~ melt-crystal separation. Second boiling could thus have over-pressured the shallow seated reservoir and triggered magma ascent ~~and eruption trigger~~ (Fig. 12c).

Without this deep ~~external~~magma transfers ~~inputs~~ we believe that the ~~little~~small reservoir ~~of~~activated in 2014 would have ~~evolved~~cooled down completely to form ~~in~~ an intrusion (~~see~~as suggested by the pervasive crystallization of the lava, one of the densest emitted from 2014 to 2017). ~~The occurrence of deep (>10 km bsl) lateral magma transfer since March April 2014 has been inferred by Boudoire et al., (2017) on the basis of deep (mantle level) seismic swarms and soil CO2 emissions on the distal western volcano flank. We suspect that these deep processes can have modified the shallower crustal stress field and favored magma vesiculation and eruption trigger (Fig. 12c).~~ The 2014 event represented ~~stead~~instead~~eed~~ the first of a long series of eruptions, whose magmas became progressively less evolved in time (Coppola et al., 2017). In this scenario the trigger mechanisms of 2014 activity are both internal and external in the sense that the ~~little~~small shallow reservoir hosting cooled magmas ~~was mature enough (due to crystallization and cooling)~~permitted to create the conditions favourable to a second boiling (Fig. 12c, and Tait et al., 1989). The second boiling was likely trigger by an almost undetectable stress field change, ~~because of the physical zonation of a mature shallow reservoir~~and was favoured by the shallow storage pressure of the magma (Fig. 12c) that promotes fast water exsolution and rapid magma response to external triggers. The second boiling ~~was~~possibly contributed to ~~than responsible for~~ the inflation registered 11 days before the eruption at 1.4-1.7 km (Fig. 12c) both by magma expansion and ~~heat~~ transfer of hot fluids to the hydrothermal system (Lénat et al., 2011). ~~. Only the summit cone was affected by short-scale and weak inflation, which has been attributed to pressurization of a very shallow magmatic source (ca. 1.4-1.7 km below volcano summit) by Peltier et al. (2016).~~

~~In this scenario we~~Our data permit to exclude (i) new magma input and/or to fluid inputs (CO2-rich fluids) from deep magmatic levels to trigger the June 2014 eruption. We also exclude (ii) heating and enhanced convection of the shallow magma reservoir (due to

~~energy~~heat diffusion~~transfer~~ without fluid or mass transfer), because this process is very slow ~~because of slow heat diffusion~~. Furthermore, ~~The~~ ~~and~~ 2014 minerals do not record evidences of ~~slow~~ magma heating. We can exclude equally that (iii) deformation of the volcanic edifice and decompression of the magma reservoir and/or hydrothermal system due to flank sliding because geodetic data show no evidence of flank sliding able to produce ~~decompression~~stress change in ~~of~~ the hydrothermal and magmatic system. ~~Geochemical (bulk rock) and petrological (mineral composition and zoning) data, permit to exclude this hypothesis. The magma erupted in 2014 results to be one of the most evolved and cold magmas ever erupted at Piton de la Fournaise (Figs 8 and 10b); it is very homogeneous (Fig. 7), minerals do not exhibit reverse zoning and their compositional evolution from phenocrysts to microlites record magma cooling and final degassing (new Figure 10a).~~ Geophysical and geochemical data have permitted to track vertical magma and fluid transfer below the volcano summit in April 2015, that is about one year after the early deep lateral magma transfer (Peltier et al., 2016). Deep processes ~~cannot be~~are difficult to ~~detected by the OVPF geodetical~~ detect for any monitoring network.

We conclude that the overpressure, caused by the second boiling, triggered the ~~The 11 days of weak summit volcano inflation, which preceded the 2014 eruption, possibly result from volatile exsolution and expansion of both the shallow magma reservoir and the hydrothermal system (Fig. 12c). We also exclude (ii) heating and enhanced convection of the shallow magma reservoir (due to energy transfer without fluid or mass transfer, because rocess is very slow because of slow heat diffusion and 2014 minerals do not record evidences of slow magma heating. We can exclude equally (iii) deformation of the volcanic edifice and decompression of the magma reservoir and/or hydrothermal system due to flank sliding because geodetic data show no evidence of flank sliding able to produce decompression of the hydrothermal and magmatic system. However, it is necessary to discuss the pressurisation (volcano inflation) and/or depressurization (volcano deflation) of the (iv) hydrothermal system located between the Dolomieu crater and the roof of the shallow magma reservoir (Fig. 12c) as a possible eruption trigger, as suggested by Lénat et al. (2011). Expansion of the hydrothermal system is due to inputs of heat and fluids from the magma reservoir or deeper and pressurization is favored by its sealing (because of mineral precipitation; lava accumulation at the volcano top). Related to this point, Froger et al., (2015) suggest that PdF hydrothermal system (and its potential sealing as well) was largely disrupted during the 2007 caldera collapse. In Lénat's model, thermal expansion of heated geothermal fluids induce rock~~

35

fracturing by pore pressure increase. Hydrothermal fracturing would cause transient decompression of the magma reservoir, thus triggering vesiculation and starting magma ascent process. However, we found no evidences of new inputs of magma or fluids in the 2014 reservoir, that would have induced the pressurization of the hydrothermal system. So, in our model the combination of change of stress field (deep input) and the physical zonation of the shallow magma reservoir promote the second boiling that enhanced the foam accumulation. Our dataset permits us to propose that the 2014 eruption was fed by a physically zoned magma reservoir with the lighter crystal poor magma erupted first (and possibly located in the upper part of the storage system) that ascends faster and feed the more energetic phase, the fountaining (Fig. 12d). This lighter magma is not more evolved than the spiny one (same bulk compositions) and it is not necessarily richer in dissolved volatile amounts; it is just poor in crystal. We conclude that the second boiling is responsible of the extraction of bubble rich melt from a crystal rich network. This last one will represent the main volume of erupted lava. eEruption. The occurrence of a hydrous almost pure melt at shallow depth permitted its fast vesiculation upon ascent towards the surface. In turn, fast ascent of the foam (Fig. 12d) hindered its crystallization and preserved high number of vesicles, high vesicularity and it is only little modified by post fragmentation expansion. Decrease in initial overpressure translated in a progressive decrease in magma ascent rate and output rate (e.g. Coppola et al., 2017 and references therein) and a temporal transition from Hawaiian activity to Strombolian activity (Fig. 12 d). Nucleation of microcrysts was enhanced in melt ascending with lower speed and in turn this syn-eruptive crystallization favoured bubble connectivity/permeability in the ascending magma, even for magma at low vesicularity and was mostly controlled by syneruptive degassing. The larger volume (dense lava) corresponds to highly-crystallized and degassed magma already in the reservoir, and experienced a slower ascent in the dyke and even further micro-crystallisation during its subaerial emplacement.

The texture of the products allowed us to follow the dynamic evolution of the system in space, (from smooth fluidal scoria emitted from rapid jet of lava fromat the fractures, to a more stable activity at the Main Vvent, and in time. At the Main Vent, in fact, we observed the transition) and in time, at the Main vent (fromfrom the golden and fluidal fragments emitted from Hawaiian fountaining, at the peak of the intensity of the eruption, to the spiny fragments, emitted from a declining Strombolian activity at the end of the eruption.)Syn-eruptive degassing is favored by bubble connectivity/permeability in the ascending magma, enhanced

by syn-eruptive crystallisation in the conduit (especially microcrysts of plg), even for magma at low vesicularity.

Therefore we here show for the first time that short lived and weak Hawaiian fountaining and Strombolian events can preserve pyroclast textures that can be considered as representing a valid approximation to magma ascent and fragmentation conditions before the explosions and correlate to the eruptive dynamics as well.

First, we found that this kind of eruption can be triggered solely by bubble accumulation and source pressurisation at a very shallow storage depth. We suggest that it is the shallow depth of the reservoir itself that allows exsolution, rather than magma cooling and evolution or recharge from a deep source. Second, these small, summit eruptions are usually related to small pockets of magma left behind following previous eruptions. Third, the thermal mechanical stratification at the reservoir level between the bubble rich portion and the more degassed and cooler one modulates the style of the explosions. Therefore, in terms of ascent and degassing history of the magma the golden and fluidal fragments represent the bubble richer and hotter portion of the melt with faster ascent rate, while the spiny fragments are the degassed, cooler portion of the reservoir, whose progressive tapping lead to a decrease in explosive intensity (from fountaining to Strombolian activity). Finally, an accumulation of olivine crystals out of equilibrium with the host magma produces minor variations in phenocryst contents with a slight increase in heavy crystals within the most degassed magma emitted toward the end of activity, as observed as a general trend at PdF (Peltier et al., 2009).

To conclude, these results highlight the importance of petrological monitoring, which can provide complementary information regarding the ongoing volcanic activity to other geophysical and geochemical monitoring tools commonly used on volcanoes.

Acknowledgements

References list

Albarède, F., and V. Tamagnan (1988), Modelling the recent geochemical evolution of the Piton de la Fournaise volcano, Réunion island, 1931-1986, *J. Petrol., 29*, 997-1030.

Albarède, F., B. Luais, G. Fitton, M.P. Semet, E. Kaminski, B.G.J Upton, P. Bachèlery, and J.L. Cheminée (1997), The geo-chemical regimes of Piton de la Fournaise Volcano Réunion. during the last 530,000 years, *J. Petrol., 38*, 171–201.

Andronico, D., M.D. Lo Castro, M. Sciotto, and L. Spina (2013a), The 2010 ash emissions at the summit craters of Mt Etna: relationship with seismo-acoustic signals, *J. Geophys. Res., 118*, 51–70, doi:10.1029/2012JB009895.

Andronico, D., J. Taddeucci, A. Cristaldi, L. Miraglia, P. Scarlato, and M. Gaeta (2013b), The 15 March 2007 paroxysm of Stromboli: video-image analysis, and textural and compositional features of the erupted deposit, Bull. Volcanol., 75, 733, doi:10.1007/s00445-013-0733-2.

Andronico, D., S. Scollo, M.D. Lo Castro, A. Cristaldi, L. Lodato, and J. Taddeucci (2014), Eruption dynamics and tephra dispersal from the 24 November 2006 paroxysm at South-East Crater, Mt Etna, Italy, *J. Volcanol. Geotherm. Res., 274*, 78–91, doi:10.1016/j.jvolgeores.2014.01.009.

Bachèlery, P., J.F. Lénat, A. Di Muro, and L. Michon (2016), Active Volcanoes of the Southwest Indian Ocean: Piton de la Fournaise and Karthala. Active Volcanoes of the World. Springer-Verlag, Berlin and Heidelberg, 1-428, DOI 10.1007/978-3-642-31395-0_12.

Boivin, P., and P. Bachèlery (2009), Petrology of 1977 to 1998 eruptions of Piton de la Fournaise, La Réunion Island, *J. Volcanol. Geotherm. Res., 184*, 109–125.

Bombrun, M., A. Harris, L. Gurioli, J. Battaglia and V. Barra (2015), Anatomy of a strombolian eruption: inferences from particle data recorded with thermal video, *J. Geophys. Res., 120*(4):2367-2387. DOI.10.1002/2014BO11556.

Boudoire, G., M. Liuzzo, A. Di Muro, V. Ferrazzini, L. Michon, F. Grassa, A. Derrien, N. Villeneuve, A. Bourdeu, C. Brunet, G. Giudice, and S. Gurrieri (2017), Investigating the deepest part of a volcano plumbing system: evidence for an active magma path below the western flank of Piton de la Fournaise (La Réunion Island), *J. Volcanol. Geotherm. Res*., doi: 10.1016/j.jvolgeores.2017.05.026.

1255 Brenguier, F., P. Kowalski, T. Staudacher, V. Ferrazzini, F. Lauret, P. Boissier, A. Lemarchand,
1256 C. Pequegnat, O. Meric, C. Pardo, A. Peltier, S. Tait, N.M. Shapiro, M. Campillo, and A. Di
1257 Muro (2012), First Results from the UnderVolc High Resolution Seismic and GPS network
1258 deployed on Piton de la Fournaise Volcano, *Seismo. Res. Lett. 83*(7),
1259 doi:10.1785/gssrl.83.1.97.

1260 Brugier, Y.A. (2016), Magmatologie du Piton de la Fournaise (Ile de la Réunion): approche
1261 volcanologique, pétrologique et expérimentale. Sciences de la Terre. Université d'Orléans,
1262 NNT: 2016ORLE2007, pp. 251.

1263 Bureau, H., F. Pineau, N. Métrich, P.M. Semet, and M. Javoy (1998a), A melt and fluid
1264 inclusion study of the gas phase at Piton de la Fournaise volcano (Reunion Island), *Chem.*
1265 *Geol. 147*, 115–130.

1266 Bureau, H., N. Métrich, F. Pineau, and M.P. Semet (1998b), Magma-conduit interaction at
1267 Piton de la Fournaise volcano (Réunion Island): a melt and fluid inclusion study, *J. Volcanol.*
1268 *Geotherm. Res. 84*, 39–60.

1269 Carey, R.J., M. Manga, W. Degruyter, D. Swanson, B. Houghton, T. Orr, and M. Patrick
1270 (2012), Externally triggered renewed bubble nucleation in basaltic magma: the 12 October
1271 2008 eruption at Halema'uma'u Overlook vent, Kīlauea, Hawai'i, USA, *J. Geophys. Res.,*
1272 *117*, B11202. doi:10.1029/2012JB009496.

1273 Carey, R.J., M. Manga, W. Degruyter, H. Gonnermann, D. Swanson D, B. Houghton, T. Orr,
1274 and M. Patrick (2013), Convection in a volcanic conduit recorded by bubbles, *Geology, 41*(4),
1275 395–398.

1276 Cashman, K.V., and M.T. Mangan (1994) Physical aspects of magmatic degassing II:
1277 constraints on vesiculation processes from textural studies of eruptive products, In: Carroll
1278 MR, Holloway JR (eds) Volatiles in magmas, Reviews in mineralogy. *Miner. Soc. Am.,*
1279 Fredricksberg, pp 447–478.

1280 Clocchiatti, R., A. Havette, and P. Nativel (1979), Relations pétrogénétiques entre les basaltes
1281 transitionnels et les océanites du Piton de la Fournaise (Ile de la Réunion, océan Indien) à
1282 partir e la composition chimique des inclusions vitreuses des olivines et des spinelles, *Bull.*
1283 *Minér., 102*, 511–525.

Colombier, M., L. Gurioli, T.H. Druitt, T. Shea, P. Boivin, D. Miallier, and N. Cluzel (2017a), Textural evolution of magma during the 9.4-ka trachytic explosive eruption at Kilian Volcano, Chaîne des Puys, France, *Bull. Volcanol., 79*(2), 1-24. doi:10.1007/s00445-017-1099-7.

Colombier, M., F.B. Wadsworth, L. Gurioli, B. Scheu, U. Kueppers, A. Di Muro, and D.B. Dingwel (2017b), The evolution of pore connectivity in volcanic rocks, *Earth Planet. Sci. Lett.*, *462*, 99-109. DOI: 10.1016/j.epsl.2017.01.011.

Colò, L., M. Ripepe, D.R. Baker, and M. Polacci (2010), Magma vesiculation and infrasonic activity at Stromboli open conduit volcano, *Earth Planet. Sc. Lett. 292*(3–4):274–280.

Coppola, D., N. Villeneuve, A. Di Muro, V. Ferrazzini, A. Peltier, M. Favalli, P. Bachèlery, L. Gurioli, A. Harris, S. Moune, I. Vlastélic, B. Galle, S. Arellano, and A. Aiuppa (2017), A Shallow system rejuvenation and magma discharge trends at Piton de la Fournaise volcano (La Réunion Island), *Earth Planet. Sci. Lett. 463*, 13-24.

Corsaro, R., and L. Miraglia (2014), The transition from summit to flank activity at Mt. Etna, Sicily (Italy): Inferences from the petrology of products erupted in 2007–2009, *J. Volcanol. Geother. Res., 275*, 51– 60.

Di Muro, A., Métrich, N., Vergani, D., Rosi, M., Armienti, P., Fougeroux, T., Deloule, E., Arienzo, I., Civetta, L. (2014), The shallow plumbing system of Piton de la Fournaise Volcano (La Réunion Island, Indian Ocean) revealed by the major 2007 caldera forming eruption, *J. Petrol., 55*, 1287-1315.

Di Muro, A., T. Staudacher, V. Ferrazzini, N. Métrich, P. Besson, C. Garofalo, and B. Villemant (2015), Shallow magma storage at Piton de la Fournaise volcano after 2007 summit caldera collapse tracked in Pele's hairs, chap 9 of Carey, R. J., V. Cayol, M. P. Poland, and D. Weis (eds.), Hawaiian Volcanoes: From Source to Surface, *American Geophysical Union Monograph 208*, pp 189–212, doi:10.1002/9781118872079.ch9.

Di Muro, A., N. Métrich, P.Allard, A. Aiuppa, M. Burton, B. Galle, and T. Staudacher (2016), Magma degassing at Piton de la Fournaise volcano, Active Volcanoes of the World, series, Springer, Bachelery, P., Lenat, J.F, Di Muro, A., Michon L., Editors. Pg. 203-222.

DYNVOLC Database (2017) Observatoire de Physique du Globe de Clermont-Ferrand, Aubière, France. DOI:10.25519/DYNVOLC-Database. Online access: http://dx.doi.org/10.25519/DYNVOLC-Database

Eychenne, J., B.F. Houghton, D.A. Swanson, R.J. Carey, and L; Swavely (2015), Dynamics of an open basaltic magma system: the 2008 activity of the Halemaʻumaʻu Overlook vent, Kīlauea Caldera. *Earth Planet. Sci. Lett., 409*, 49–60.

Famin, V., B. Welsch, S. Okumura, P. Bachèlery, and S. Nakashima (2009), Three differentiation stages of a single magma at Piton de la Fournaise (Réunion hotspot). *Geoch. Geoph. Geos. 10*, Q01007. doi:10. 1029/2008GC002015.

Fisk, M.R., B.G.J Upton, C.E. Ford, and W.M. White (1988), Geochemical and experimental study of the genesis of magmas of Reunion island, Indian Ocean, *J. Geophys. Res., 93*, 4933-4950.

Formenti, Y, and T.H. Druitt (2003), Vesicle connectivity in pyroclasts and implications for the fluidisation of fountain-collapse pyroclastic flows, Montserrat (West Indies), *Earth Planet. Sci. Lett., 214*, 561–574.

Gardner, J.E., R.M.E. Thomas, C. Jaupart, and S. Tait (1996), Fragmentation of magma during Plinian volcanic eruptions, *Bull. Volcanol., 58*, 144–162.

Giachetti, T., T.H. Druitt, A. Burgisser, L. Arbaret, and C. Galven (2010), Bubble nucleation and growth during the 1997 Vulcanian explosions of Soufrière Hills Volcano, Montserrat, *J. Volcanol. Geotherm. Res., 193*(3–4):215–231. doi:10.1016/j.jvolgeores.2010.04.001.

Gonnermann, H.M., and M. Manga (2013) Dynamics of magma ascent in the volcanic conduit. In: Fagents, S.A., Gregg, T.K.P., Lopes, R.M.C. (Eds.), Modeling Volcanic Processes: The Physics and Mathematics of Volcanism. Cambridge University Press, Cambridge.

Gurioli, L., A.J.L. Harris, B.F. Houghton, M. Polacci, and M. Ripepe (2008) Textural and geophysical characterization of explosive basaltic activity at Villarica volcano, *J. Geophys. Res., 113*, B08206. doi:10.1029/2007JB005328

Gurioli, L., A.J.L. Harris, L. Colo, J. Bernard, M. Favalli, M. Ripepe, and D. Andronico (2013), Classification, landing distribution and associated flight parameters for a bomb field emplaced during a single major explosion at Stromboli, Italy, *Geology, 41*, 559-562, DOI 10.1130/G33967.1.

Gurioli, L., L. Colo', A.J. Bollasina, A.J.L. Harris, A. Whittington, and M. Ripepe (2014), Dynamics of strombolian explosions: inferences from inferences from field and laboratory

studies of erupted bombs from Stromboli volcano, *J. Geophys. Res., 119*(1), DOI:10.1002/2013JB010355.

Gurioli, L., D. Andronico, P. Bachelery, H. Balcone-Boissard, J. Battaglia, G. Boudon, A. Burgisser, S.B. M.R. Burton, K. Cashman, S. Cichy, R. Cioni, A. Di Muro, L. Dominguez, C. D'Oriano, T. Druitt, A.J.L Harris, M. Hort, K. Kelfoun, J.C. Komorowski, U. Kueppers, J.L. Le Pennec, T. Menand, R. Paris, L. Pioli, M. Pistolesi, M. Polacci, M. Pompilio, M. Ripepe, O. Roche, E. Rose-Koga, A. Rust, L. Scharff, F. Schiavi, R. Sulpizio, J. Taddeucci, and T. Thordarson (2015), MeMoVolc consensual document: a review of cross-disciplinary approaches to characterizing small explosive magmatic eruptions, *Bull. Volcanol., 77*, 49. DOI: 10.1007/s00445-015-0935-x.

Hammer, J.E., K.V. Cashman, R.P. Hoblitt, and S. Newman (1999) Degassing and microlite crystallization during pre-climactic events of the 1991 eruption of Mt. Pinatubo, Philippines, *Bull. Volcanol. 60*, 355–380.

Harris, A.J.L., N. Villeneuve, A. Di Muro, V. Ferrazzini, A. Peltier, D. Coppola, M. Favalli, P. Bachèlery, J.-L. Foger, L. Gurioli, S. Moune, I. Vlastélic, B. Galle, and S. Arellano (2017), Effusive Crises at Piton de la Fournaise 2014-2015: A Review of a Multi-National Response Model, *Applied Volcanology, 6,* 11, DOI 10.1186/s13617-017-0062-9

Helz, R.T., and C.R. Thornber (1987), Geothermometry of Kilauea Iki lava lake, Hawaii, *Bull. Volcanol., 49*, 651–668.

Hibert, C, A. Mangeney, M. Polacci, A. Di Muro, S. Vergniolle, V. Ferrazzini, B. Taisne, M. Burton, T. Dewez, G. Grandjean, A. Dupont, T. Staudacher, F. Brenguier, N.M. Shapiro, P. Kowalski, P. Boissier, P. Catherine, and F. Lauret (2015), Multidisciplinary monitoring of the January 2010 eruption of Piton de la Fournaise volcano, La Réunion island, *J. Geophis. Res., 120*(5), 3026-3047

Higgins M.-D. (2000). Measurement of crystal size distributions, *American Mineralogist, 85*, 1105-1116.

Houghton, B.F., and C.J.N. Wilson (1989), A vesicularity index for pyroclastic deposits, *Bull. Volcanol., 51*, 451–462. doi:10.1007/BF01078811

Houghton, B.F., D.A. Swanson, R.J. Carey, J Rausch., and A.J Sutton (2011), Pigeonholing pyroclasts, insights from the 19 March 2008 explosive eruption of Kīlauea volcano, *Geology,39*, 263–266, doi:10.1130/G31509.1.

Houghton, B.F., D.A. Swanson, J. Rausch, R.J. Carey, Fagents S.A., and T.R. Orr (2013), Pushing the volcanic explosivity index to its limit and beyond: constraints from exceptionally weak explosive eruptions at Kılauea in 2008, *Geology, 41*(6):627–630

Houghton, B.F., J. Taddeucci, D. Andronico, H.M. Gonnermann, M. Pistolesi, M.R. Patrick, T.R. Orr, D.A. Swanson, M.Edmonds, D. Gaudin, R.J. Carey and P. Scarlato (2016), Stronger or longer: Discriminating between Hawaiian and Strombolian eruption styles, *Geology* doi: 10.1130/G37423.1

Inman, D.L. (1952) Measures for describing the size distribution of sediments, *J. Sed. Petrol., 22, 125–145.*

Kahl, M., S.Chakraborty, M. Pompilio, and F. Costa (2015), Constraints on the nature and evolution of the magma plumbing system of Mt. Etna Volcano (1991–2008) from a combined thermodynamic and kinetic modelling of the compositional record of minerals, *J.Petrol., 56*, 2025–2068, doi:10.1093/petrology/egv063.

Kawabata, E., S.J. Cronin, M.S. Bebbington, M.R.H. Moufti, N. El-Masry, and T. Wang (2015), Identifying multiple eruption phases from a compound tephra blanket: an example of the AD1256 Al-Madinah eruption, Saudi Arabia, *Bull. Volcanol., 77*, 6 DOI 10.1007/s00445-014-0890-y.

Lange, R.A.̶.̶L̶.̶, H.M. Frey, and J. Hector (2009), A thermodynamic model for the plagioclase-liquid hygrometer/thermometer, *Am. Mineral., 94*, 494–506.

Lautze, N., J. Taddeucci, D. Andronico, C. Cannata, L. Tornetta, P. Scarlato, B. Houghton, and D. Lo Castro (2012), SEM-based methods for the analysis of basaltic ash from weak explosive activity at Etna in 2006 and the 2007 eruptive crisis at Stromboli, *Phys. Chem. Earth 45*,46, 113–127, doi:10.1016/j.pce.2011.02.001.

Leduc, L., L. Gurioli, A.J.L. Harris, L. Colo', and E. Rose-Koga (2015), Types and mechanisms of strombolian explosions: characterization of a gas-dominated explosion at Stromboli, *Bull. Volcanol., 77*, 8, DOI: 10.1007/s00445-014-0888-5

1400 Leibrandt, S, and J.L. Le Pennec (2015), Towards fast and routine analyses of volcanic ash
1401 morphometry for eruption surveillance applications, *J. Volcanol. Geotherm. Res., 297*, 11–27.

1402 Lénat, J.-F., P. Bachèlery, and A. Peltier (2011), The interplay between collapse structures,
1403 hydrothermal systems and magma intrusions: the case of the central area of Piton de la
1404 Fournaise volcano, *Bull. Volc.* doi:10.1007/s00445-011-0535-3

1405 Lénat, E.F., P.B. Bachelery, and O. Merle (2012), Anatomy of Piton de la Fournaise volcano
1406 (La Réunion, Indian Ocean), *Bull. Volcanol. 74*, 1945–1961.

1407 Lengliné, O, Z. Duputel, and V. Ferrazzini (2016), Uncovering the hidden signature of a
1408 magmatic recharge at Piton de la Fournaise volcano using small earthquakes, *Geophys. Res.*
1409 *Lett., 43*, doi: 10.1002/2016GL068383

1410 Lindoo, A., J.F. Larsen, K.V. Cashman, A.L. Dunn, and O.K Neill (2016), An experimental
1411 study of permeability development as a function of crystal-free melt viscosity, *Earth Planet.*
1412 *Sci. Lett., 435*, 45–54, doi: 10 .1016 /j .epsl .2015 .11 .035.

1413 Lindoo, A., J.F. Larsen, K.V. Cashman, and J. Oppenheimer (2017), Crystal controls on
1414 permeability development and degassing in basaltic andesite magma, *Geology, 45*(9), p. 831-
1415 834.

1416 Liuzzo, M., Di Muro, A., Giudice, G., Michon, L., Ferrazzini, V., and Gurrieri, S. (2015), New
1417 evidence of CO_2 degassing anomalies on the Piton de la Fournaise volcano and the link with
1418 volcano tectonic structures Geochemistry, Geophysics, Geosystems, 16, doi:10.1002/
1419 2015GC006032.

1420 Mangan, M.T., and K.V. Cashman (1996), The structure of basaltic scoria and reticulite and
1421 inferences for vesiculation, foam formation, and fragmentation in lava fountains. *J. Volcanol.*
1422 *Geotherm. Res., 73*, 1–18.

1423 Menand, T., and J.C. Phillips (2007), Gas segregation in dykes and sills. *J. Volcanol. Geother.*
1424 *Res.*, *159*(4), 393–408. https://doi.org/10.1016/j.jvolgeores.2006.08.003.

1425 Michon, L., A. Di Muro, N. Villeneuve, C. Saint-Marc, P. Fadda, and F. Manta (2013),
1426 Explosive activity of the summit cone of Piton de la Fournaise volcano (La Réunion Island): a
1427 historical and geological review, *J. Volcanol. Geotherm. Res. 263*, 117-133.

44

Moitra, P., H.M. Gonnermann, B.F. Houghton, and T. Giachetti (2013), Relating vesicle shapes in pyroclasts to eruption styles, *Bull. Volcanol.* 75, 691. doi:10.1007/s00445-013-0691-8

Morgan D.J., and D.A. Jerram (2006), On estimating crystal shape for crystal size distribution analysis, *J. Volc. Geotherm. Res., 154*, 1–7.

Moune, S., O. Sigmarsson, P. Schiano, T. Thordarson, and J.K. Keiding (2012), Melt inclusion constraints on the magma source of Eyjafjallajökull 2010 flank eruption, *J. Geophys. Res., 117*, B00C07, doi:10.1029/2011jb008718.

Morandi, A., C. Principe, A. Di Muro, G. Leroi, L. Michon, and P. Bachèlery (2016), Pre-historic explosive activity at Piton de La Fournaise volcano. In: Bachèlery P, Lénat JF, Di Muro A, Michon L (eds) Active Volcanoes of the Southwest Indian Ocean: Piton de la Fournaise and Karthala. Active Volcanoes of the World. Springer-Verlag, Berlin and Heidelberg, pp 107–138

Óladóttir, B., O. Sigmarsson, G. Larsen, and J.-L. Devidal (2011), Provenance of basaltic tephra from Vatnajökull subglacial volcanoes, Iceland, as determined by major- and trace-element analyses, *Holocene, 21*, 1037–1048, doi:10.1177/0959683611400456.

Oppenheimer, J., A.C. Rust, K.V. Cashman, and B. Sandnes (2015), Gas migration regimes and outgassing in particle-rich suspensions, *Frontiers in Physics, 3*, 1–13, doi: 10 .3389 /fphy .2015 .00060.

Ort, M.H., A. Di Muro, L. Michon, and P. Bachèlery (2016), Explosive eruptions from the interaction of magmatic and hydrothermal systems during flank extension: the Bellecombe Tephra of Piton de La Fournaise (La Réunion Island), *Bull. Volcanol. 78*, 5, doi:10.1007/s00445-015-0998-8.

Papale P., R. Moretti, and D. Barbato (2006), The compositional dependence of the saturation surface of $H_2O + CO_2$ fluids in silicate melts, *Chemical Geology*, 229, 1/3, 78-95, doi:10.1016/j.chemgeo.2006.01.013.

Parcheta, C.E., B.F. Houghton, and D.A. Swanson (2013), Contrasting patterns of vesiculation in low, intermediate, and high Hawaiian fountains: a case study of the 1969 Mauna Ulu eruption, *J. Volcanol. Geotherm. Res., 255*, 79–89

Peltier, A., P. Bachèlery, and T. Staudacher (2009), Magma transport and storage at Piton de la Fournaise (La Réunion) between 1972 and 2007: A review of geophysical and geochemical data. *J. Volcanol.Geother. Res., 184,* 93-108.

Peltier, A., F. Beauducel, N. Villeneuve, V. Ferrazzini, A. Di Muro, A. Aiuppa, A. Derrien, K. Jourde, and B. Taisne (2016), Deep fluid transfer evidenced by surface deformation during the 2014–2015 unrest at Piton de la Fournaise volcano, *J. Volcanol. Geotherm. Res., 321*, 140–148. http://dx.doi.org/10.1016/j.jvolgeores.2016.04.031.

Peltier, A., P. Bachèlery, and T. Staudacher (2009), Magma transport and storage at Piton de la Fournaise (La Réunion) between 1972 and 2007: A review of geophysical and geochemical data. *J. Volcanol.Geother. Res., 184,* 93-108.

Polacci, M., R. Corsaro, and D. Andronico (2006a), Coupled textural and compositional characterization of basaltic scoria: insights into the transition from Strombolian to fire fountain activity at Mount Etna, Italy, *Geology, 34*(3), 201–204. doi:10.1130/G223181.1.

Polacci, M., C. Bouvet de Maisonneuve, D. Giordano, M. Piochi, L. Mancini L., W. Degruyter, and O. Bachmanng (2014), Permeability measurements of Campi Flegrei pyroclastic products: an example from the Campanian Ignimbrite and Monte Nuovo eruptions. *J. Volcanol. Geotherm. Res. 272*, 16–22.

Putirka, K.D. (2008), Thermometers and barometers for volcanic systems, *Rev. Mineral. Geochem. 69*, 61-120.

Roeder, P., E. Gofton, and C. Thornber (2006), Cotectic proportions of olivine and spinel in olivine-tholeiitic basalt and evaluation of pre-eruptive processes, *J. Petrol., 47*, 883-900.

Roult, G., A. Peltier, T. Staudacher, V. Ferrazzini, B. Taisne, A. Di Muro, and The OVPF Team (2012), A comprehensive classification of the Piton de la Fournaise eruptions (La Réunion Island) spanning the 1986–2010 period. Search for eruption precursors from the broad-band GEOSCOPE RER station analysis and interpretation in terms of volcanic processes, *J. Volcanol. Geotherm. Res., 241*, 78–104.

Rust, A.C., and K.V. Cashman (2011), Permeability controls on expansion and size distributions of pyroclasts, *J. Geophys. Res., 116*, B11202.

Saar, M.O., M. Manga, K.V. Cashman, and S. Fremouw (2001) Numerical models of the onset of yield strength in crystal-melt suspensions: *Earth Planet. Sci. Lett., 187,* 367–379, doi: 10 .1016 /S0012 -821X (01)00289 -8.

Salaün, A., Villemant, B., Semet, M.P., and T. Staudacher (2010), Cannibalism of olivine-rich cumulate xenoliths during the 1998 eruption of Piton de la Fournaise (La Réunion hotspot): Implications for the generation of magma diversity. *J.Volcanol. Geother. Res., 198*, 187-204.

Schiano, P., K. David, I. Vlastélic, A. Gannoun, M. Klein, F. Nauret, and Bonnand P. (2012), Osmium isotope systematics of historical lavas from Piton de la Fournaise (Réunion Island, Indian Ocean), *Contrib. Mineral. Petrol.,* http://dx.doi.org/10.1007/s00410-012-0774-0.

Shea, T., (2017) Bubble nucleation in magmas: a dominantly heterogeneous process? *J. Volcanol. Geotherm. Res. 343,* 155–170.

Shea, T., B.F. Houghton, L. Gurioli, K.V. Cashman, J.E. Hammer, and B. Hobden (2010), Textural studies of vesicles in volcanic rocks: an integrated methodology, *J. Volcanol. Geotherm. Res., 190*, 271–289.

Shea, T., L. Gurioli, and B.F. Houghton (2012), Transitions between fall phases and pyroclastic density currents during the AD 79 eruption at Vesuvius: building a transient conduit model from the textural and volatile record, *Bull. Volcanol., 74*, 2363–2381, doi:10.1007/s00445-012-0668-z.

Shea, T., (2017) Bubble nucleation in magmas: a dominantly heterogeneous process? *J. Volcanol. Geotherm. Res. 343,* 155–170.

Sparks, R.S.J. (1978), The dynamics of bubble formation and growth in magmas: a review and analysis, *J. Volcanol. Geotherm. Res., 3*, 1–37.

Sparks, R.S.J. (2003). Forecasting volcanic eruptions, *Earth Planet. Sci. Lett., 210*, 1–15.

Spina, L., C. Cimarelli, B. Scheu, D. Di Genova, and D. B. Dingwell (2016) On the slow decompressive response of volatile- and crystal-bearing magmas: An analogue experimental investigation, *Earth Planet. Sci. Lett., 433*, 44-53.

Staudacher, T., and A. Peltier (2015), Ground deformation at Piton de la Fournaise (La Réunion Island), a review from 20 years of GNSS monitoring, In: Bachèlery P, Lénat, JF, Di Muro A, Michon L (ed) Active volcanoes of the Southwest Indian Ocean: Piton de la

Fournaise and Karthala. Active volcanoes of the world. Springer, Berlin, 139-170. doi:10.1007/978-3-642-31395-0_9

Staudacher, T., V. Ferrazzini, A. Peltier, P. Kowalski, P. Boissier, P. Catherine, F. Lauret, and F. Massin (2009), The April 2007 eruption and the Dolomieu crater collapse, two major events at Piton de la Fournaise (La Re¤union Island, Indian Ocean). *J. Volcanol. Geother. Res. 184*, 126-137, doi:10.1016/j.jvolgeores.2008.11.005.

Stovall, W.K., B.F. Houghton, H.M. Gonnermann, S.A. Fagents, and D.A. Swanson (2011), Eruption dynamics of Hawaiian-style fountains: the case study of episode 1 of the Kīlauea Iki 1959 eruption, *Bull. Volcanol. 73*, 511–529. doi:10.1007/s00445-010-0426-z.

Stovall, W.K., B.F. Houghton, J.E. Hammer, S.A. Fagents, and D.A. Swanson (2012), Vesiculation of high fountaining Hawaiian eruptions: episodes 15 and 16 of 1959 Kīlauea Iki, *Bull. Volcanol., 74*, 441–455, doi:10.1007/s00445-011-0531-7.

Swanson, D.A., K. Wooten, and T. Orr (2009), Buckets of ash track tephra flux from Halemaʻumaʻu crater, Hawaiʻi. *Eos Trans. AGU, 90*, 427–428. doi:10.1029/2009EO460003.

Taddeucci, J., M. Pompilio, and P. Scarlato (2002), Monitoring the explosive activity of the July–August 2001 eruption of Mt. Etna (Italy) by ash characterization, *Geophys. Res. Lett., 29*(8), 1029–1032. doi:10. 1029/2001GL014372.

Tait, S., C. Jaupart, and S. Vergniolle (1989), Pressure, gas content and eruption periodicity of a shallow, crystallising magma chamber, *Earth Planet. Sci. Lett., 92*, 107-123.

Takeuchi, S., S. Nakashima, and A. Akihiko Tomiya (2008) Permeability measurements of natural and experimental volcanic materials with a simple permeameter: toward an understanding of magmatic degassing processes, *J. Volcanol. Geotherm. Res.*, 177:329–339.

Thornber, C.R., K. Hon, C. Heliker, and D.A. Sherrod (2003), A Compilation of Whole-Rock and Glass Major-Element geochemistry of Kīlauea Volcano, Hawai'i, near-vent eruptive products: January 1983 through September 2001: *U.S.G.S. Open File Report*, *03*-477.

Thordarson, T, S Self, N Óskarsson, and T Hulsebosch (1996), Sulfur, chlorine and fluorine degassing and atmospheric loading by the 1783–1784 AD Laki (Skaftár Fires) eruption in Iceland, *Bull. Volcanol. 58*, 205–225.

48

1542 Villemant, B., A. Salaün, and T. Staudacher (2009), Evidence for a homogeneous primary
1543 magma at Piton de la Fournaise (La Réunion): A geochemical study of matrix glass, melt
1544 inclusions and Pélé's hairs of the 1998–2008 eruptive activity, *J. Volcanol. Geotherm. Res.,*
1545 *184*, 79–92.

1546 Vlastélic, I., and A.J. Pietruszka (2016), A review of the recent geochemical evolution of
1547 Piton de la Fournaise Volcano (1927–2010). In: Bachèlery, P., Lénat, J.F., Di Muro, A.,
1548 Michon, L. (Eds.), Active Volcanoes of the Southwest Indian Ocean. In: Active Volcanoes of
1549 the World, pp.185–201.

1550 ~~Vlastélic, I., T. Staudacher, and M. Semet (2005), Rapid change of lava composition from~~
1551 ~~1998 to 2002 at Piton de la Fournaise (Réunion) inferred from Pb isotopes and trace elements:~~
1552 ~~evidence for variable crustal contamination, *J. Petrol. 46*, 79-107.~~

1553 Vlastélic, I., A. Peltier, and T. Staudacher (2007), Short-term (1998–2006) fluctuations of Pb
1554 isotopes at Piton de la Fournaise volcano (Réunion Island): origins and constraints on the size
1555 and shape of the magma reservoir, *Chem. Geology, 244*, 202-220.

1556 Vlastélic, I., C. Deniel, C. Bosq, P. Telouk, P. Boivin, P. Bachèlery, V. Famin,. and T.
1557 Staudacher (2009), Pb isotope geochemistry of Piton de la Fournaise historical lavas, *J.*
1558 *Volcanol. Geother. Res., 184*, 63-78.

1559 Vlastélic, I., T. Staudacher, P. Bachèlery, P. Télouk, D. Neuville., and M. Benbakkar (2011)
1560 Lithium isotope fractionation during magma degassing: constraints from silicic differentiates
1561 and natural gas condensates from Piton de la Fournaise volcano (Réunion Island), *Chemical*
1562 *Geology, 284*, 26–34.

1563 Vlastélic, I., G. Menard, M. Gannoun, J.-L Piro., T Staudacher, and V. Famin (2013), Magma
1564 degassing during the April 2007 collapse of Piton de la Fournaise: the record of semi-volatile
1565 trace elements (Li, B, Cu, In, Sn, Cd, Re, Tl, Bi), *J. Volcanol. Geother. Res., 254*, 94-107.

1566 Vlastélic, I., A. Gannoun, A. Di Muro, L. Gurioli, P. Bachèlery, and J.M. Henot (2016), Origin
1567 and fate of sulfide liquids in hotspot volcanism (La Réunion): Pb isotope constraints from
1568 residual Fe–Cu oxides, *Geochim. Cosmochim. Acta, 194*, 179-192.

1569 Welsch, B., F. Faure, P. Bachèlery, and V. Famin (2009), Microcrysts record transient
1570 convection at Piton de la Fournaise volcano (La Réunion Hotspot), *J. Petrol., 50*, 2287-2305.

1571   Welsch, B., V. Famin, A. Baronnet, and P. Bachèlery (2013), Dendritic crystallization: a single

1572   process for all textures of olivine in basalts? *J. Petrol., 54*, 539-574.

1573   White, J.D.L., and B.F. Houghton (2006), Primary volcaniclastic rocks, *Geology, 34*, 677–

1574   680, doi:10.1130/G22346.1.

1575   **Figure captions**

1576

1577
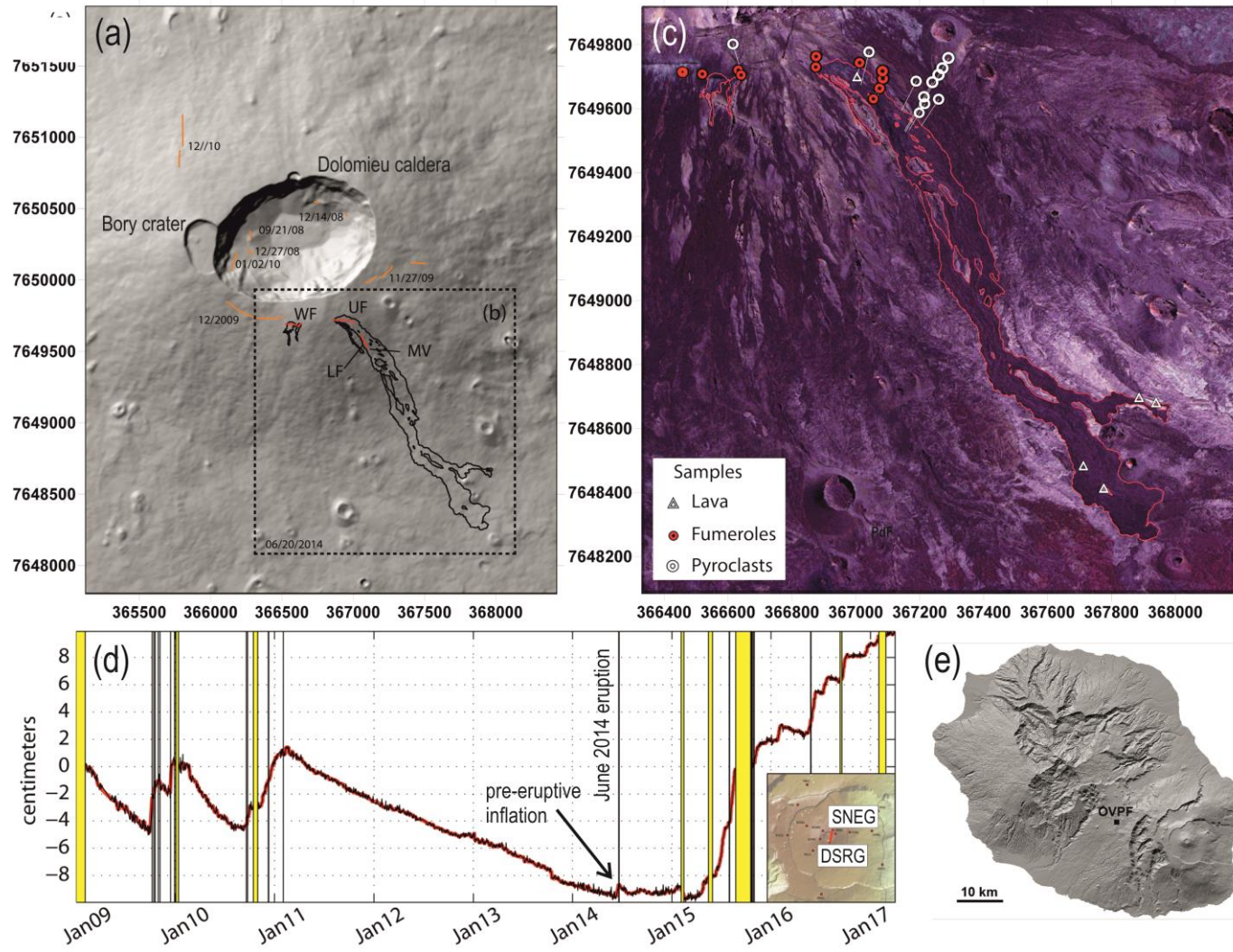
1579

1580 **Figure 1** a) Digital elevation model of the summit crater area at Piton de la Fournaise, La Réunion, France; orange = fractures generated by pre-
1581 2014 eruptions (reported are the dates of their activities); b) red = fractures active during the 2014 eruption: WF (western fracture), UF (upper
1582 fracture), LF (lower fracture), MV (Main Vent). Black= outline of the 2014 lava field; c) locations of sample collection points. The coordinates
1583 are in UTM, zone 40 south. (d) Distance change (baseline) in centimetres between two GNSS summit stations: DSRG and SNEG (see location in
1584 the inset). Increase and decrease of the signal mean a summit inflation and deflation, respectively. The yellow areas represent eruptive and
1585 intrusive periods. In this figure, the rapid and strong variations linked to dike injections preceding intrusions and eruptions by a few tens of
1586 minutes have been removed; (e) Digital Elevation Model of La Réunion island.

1587

1588

52

June 2014 eruption at PdF

Early morning, June 21

a)

b)

June 21 ~ 7h00

c)

June 21, 7h38

d)

June 21, 13h35

e)

June 21,17h00

f)

g)

June 2014 eruption at PdF

Early morning, June 21
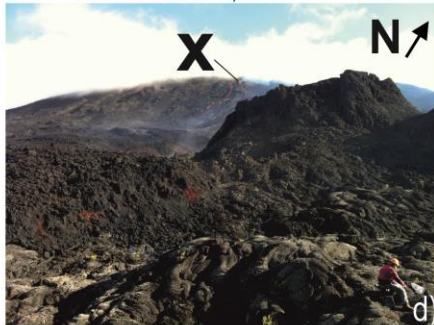
June 21, 13h35
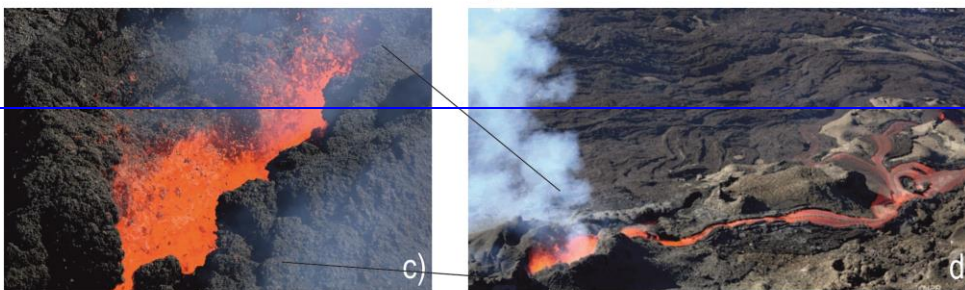
June 21,17h00

Figure 2 Photos collection from the ~~web site~~2014 eruption of the Main Vent, highlighted with a white cross (see location in Fig. 1). From a to ~~g~~f: evolution of the Strombolian activity from early morning to evening, June 21 that shows ~~.~~ a decline in the activity with time. Unfortunately, the more energetic fountaining events that happened during the night were not documented. a) Strombolian activity at the Main Vent and associated lava flow; b) zoom view of the Strombolian activity at the Main Vent. ~~All the photos are from the Main Vent (see Fig. 1).~~ The images in a, b and the inset in b are from Laurent Perrier; c) aerial view of the SE flank of the PdF, taken by the OVPF team from the helicopter of the gendarmerie of PdF; d)

eastern front of the lava where the OVPF team collected a quenched lava sample; e) low Strombolian activity at the Main Vent and the associated lava flow, photo from: http://www.rtl.fr/actu/sciences-environnement/la-reunion-eruption-du-piton-de-la-fournaise-apres-4-ans-de-sommeil-7772778861; d) http://www.ipreunion.com/volcan/reportage/2014/06/21/eruption-du-piton-de-la-fournaise-actualise-a-17h-la-lave-coule-sur-1-5-kilometre,26023.html; fe) and g) decline of the Strombolian activity at the Main Vent, the photo in e) is from http://www.zinfos974.com/L-eruption-du-Piton-de-la-Fournaise-Le-point-de-17h_a72981.htmlhttp://www.zinfos974.com/L-eruption-du-Piton-de-la-Fournaise-Le-point-de-17h_a72981.html; and the photo if f) is from: f) http://nancyroc.com/eruption-a-la-reunion
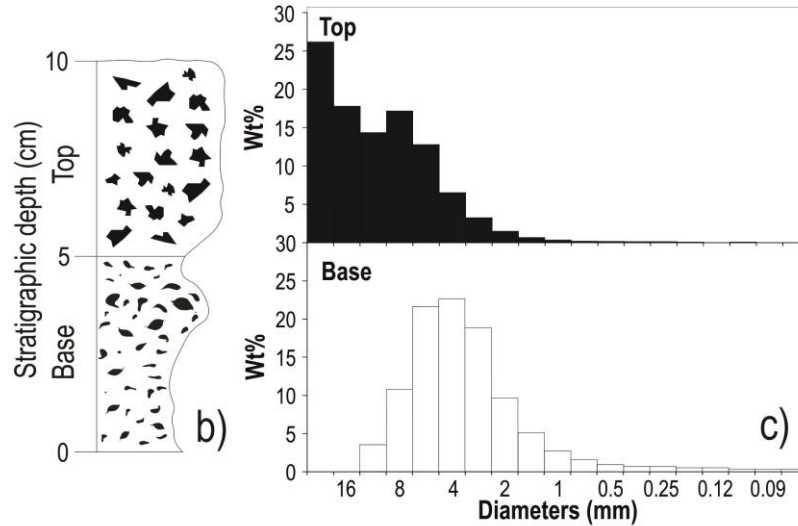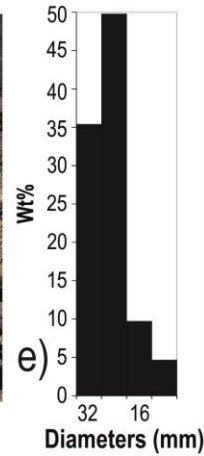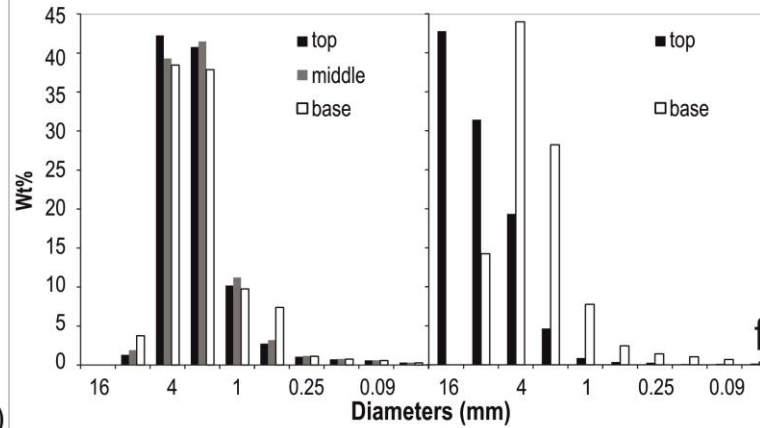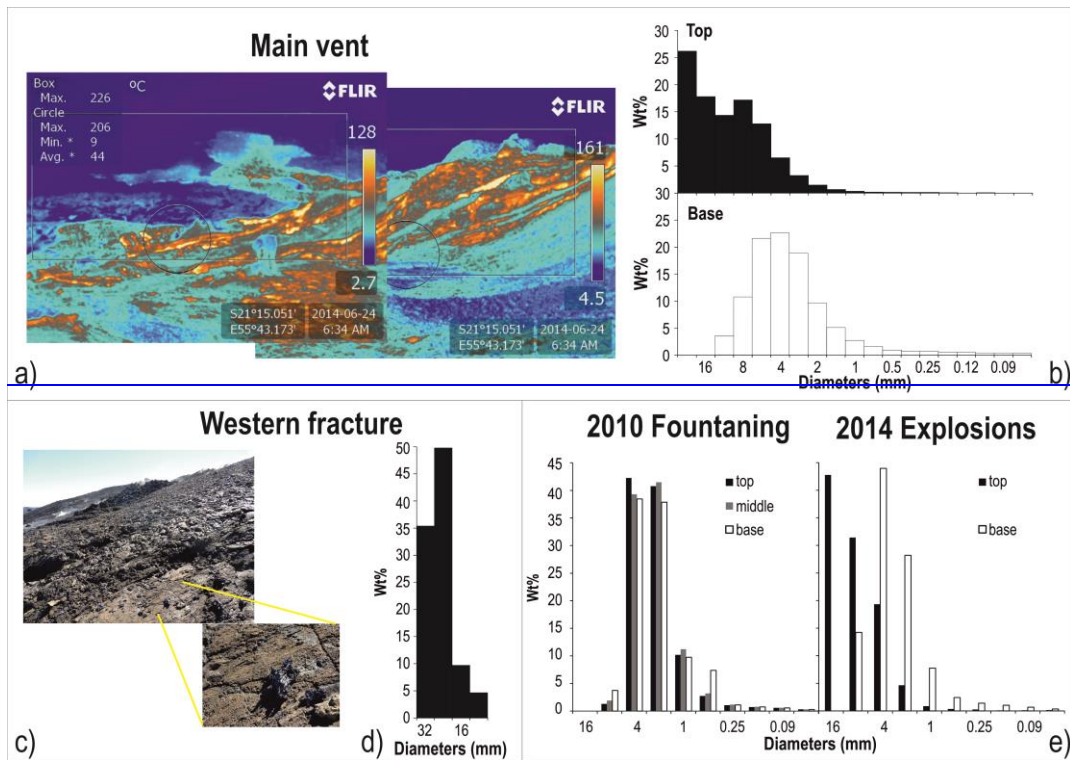
Figure 3 a) Continuous blanket of scoria fall out deposit emitted from the Main Vent during June 2014 eruption at PdF. The black cross locates the position of the Main Vent (see Fig. 1 for the location); b) schematic stratigraphycal log of the scoria fall out deposit emplaced during June 2014 eruption. Thermal photo of the scoria fall out area in proximity to the Main Vent (see Fig. 1 for the location); bc) grain size histograms forof the base and the top of the deposit of the Main Vent, the particle diameters are at half phi; de) scattered scoria (outlined in yellow) from the Western Fracture (see Fig. 1 for the location); ed) grain size histogram of the scoria deposit at the Western Fracture, the particle diameters are in

57

full phi; fe) comparison between the grain size histograms for the 2010 Hawaiian fountaining and the 2014 Main vent activity, both the particle axes are reported in full phi for comparison.
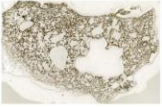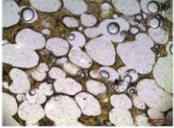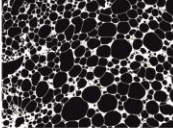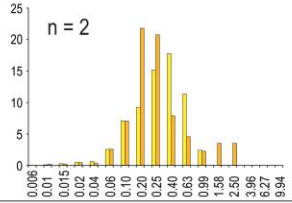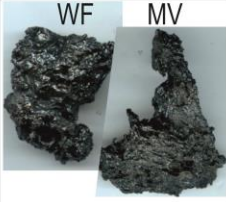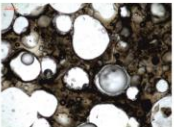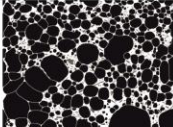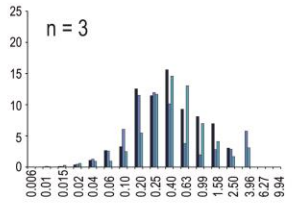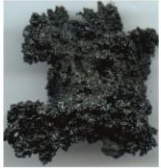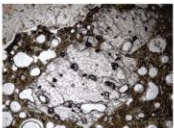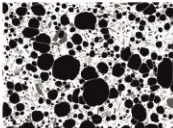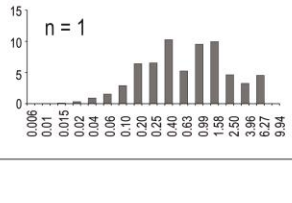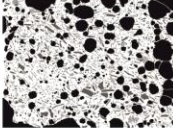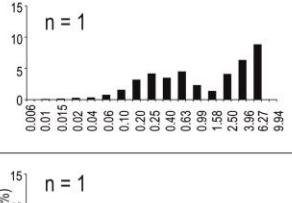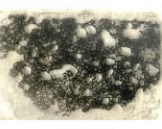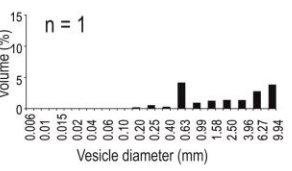
Type	Clast	Thin section	Microscope	SEM (25X)	VSD	Crystal vol %	N_v
Golden Pumice (a)			0.02 mm		n = 2	Tot = 8-15 Mplg= rare μplg = 6-11 Mcpx = rare μcpx =(1-3)	2×10^7 9×10^6
Fluidal Scoria (b)	WF MV		0.02 mm		n = 3	Tot = 4-23 Mplg = 0.4-1 μplg = 2-19 Mcpx = 0-1 μcpx = 1-4	2×10^7 5×10^6 3×10^6
Spiny glassy scoria (c)			0.02 mm		n = 1	Tot = 51 Mplg = 11 μplg = 23 Mcpx =15 μcpx = 2	6×10^6
Spiny opaque scoria (d)	1 cm				n = 1	Tot = 55 Mplg = 11 μplg = 25 Mcpx = 10 μcpx = 9	4×10^6
Lava (e)	1m	1 cm	0.02 mm	1 mm	n = 1	Tot = 100 Mplg = 2 μplg = 64 Mcpx = 3 μcpx = 31	2×10^4

Volume (%) — Vesicle diameter (mm)

Figure 4 Textural features of June 2014 pyroclasts and lava. Clast = photo of the different types of juvenile pyroclasts and lava channel. The photo of the lava channel is from Laurent Perrier. WF = Western Fracture (smooth fluidal scoria), MV = Main Vent (fluidal scoria, less smooth than the ons at the WF),. Thin section = thin section imaged with a desktop scanner. Microscope = photo taken with an optical microscope using natural light; SEM (25X) = photo captured using a scanning electron microscopy (SEM), in BSE mode at 25x magnification: black are vesicles, white is glass, grey are crystals. VSD = vesicle volume distribution histograms, where the diameter, in mm, is plotted versus the volume percentage, n = number of measured clasts; Crystal vol. % : Tot = total percentage of crystals corrected for the vesicularity; Mplg = percentage of mesocrysts of plagioclase; µplg = percentage of microcrysts of plagioclase; Mcpx = percentage of mesocrysts of pyroxene; µcpx = percentage of microcrysts of pyroxene; Nv = number density corrected for the vesicularity.

60

1652

1653

1654

61
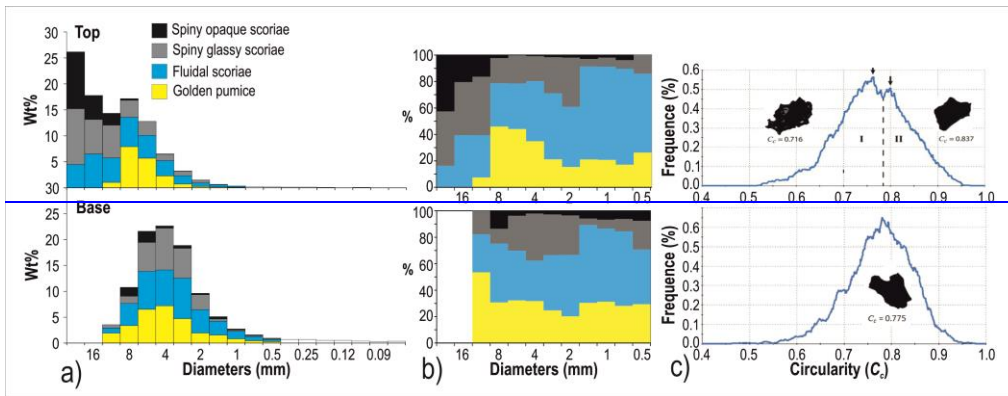
Figure 5 Proportion of each type of clast measured ~~from the Main Cone~~ from the base to the top of the 10 cm thick deposit emplaced during the eruption, at the Main Vent site. The deposit is dominated by Hawaiian-like lapilli fragments at the base (golden pumice and fluidal scoria) and Strombolian-like bombs and lapilli at the top (spiny scoria)~~for the 2014 eruption~~: (a) componentry within the different grain size classes ~~from the base to the top of a 10 cm thick scoria deposit~~; b) normalized componentry composition from the base to the top of the deposits.

~~; (c) Morphologi G3 results for the coarse ash fragments (350 micron), where the population is formed exclusively of smooth fragments that correspond to fluidal and golden pumice.~~
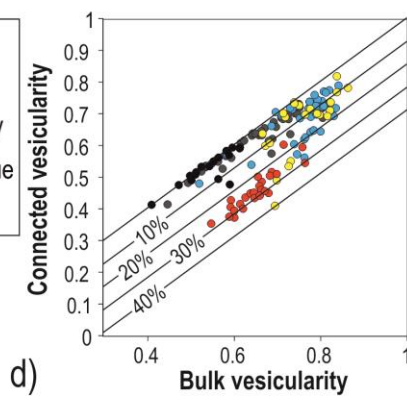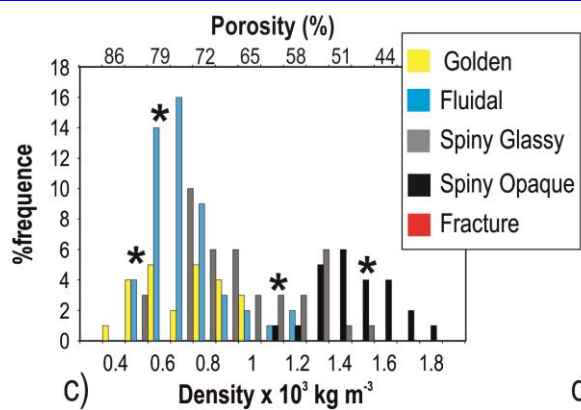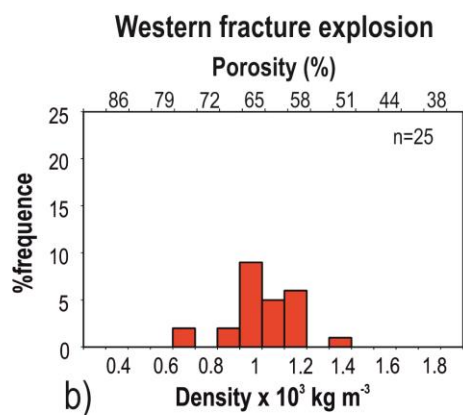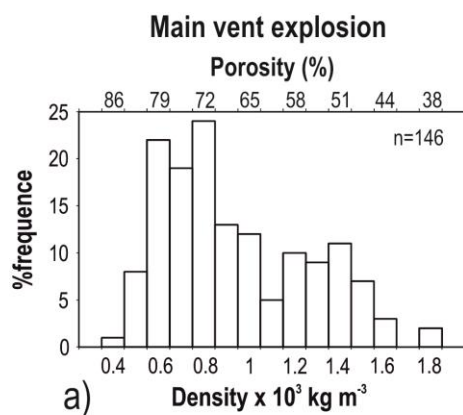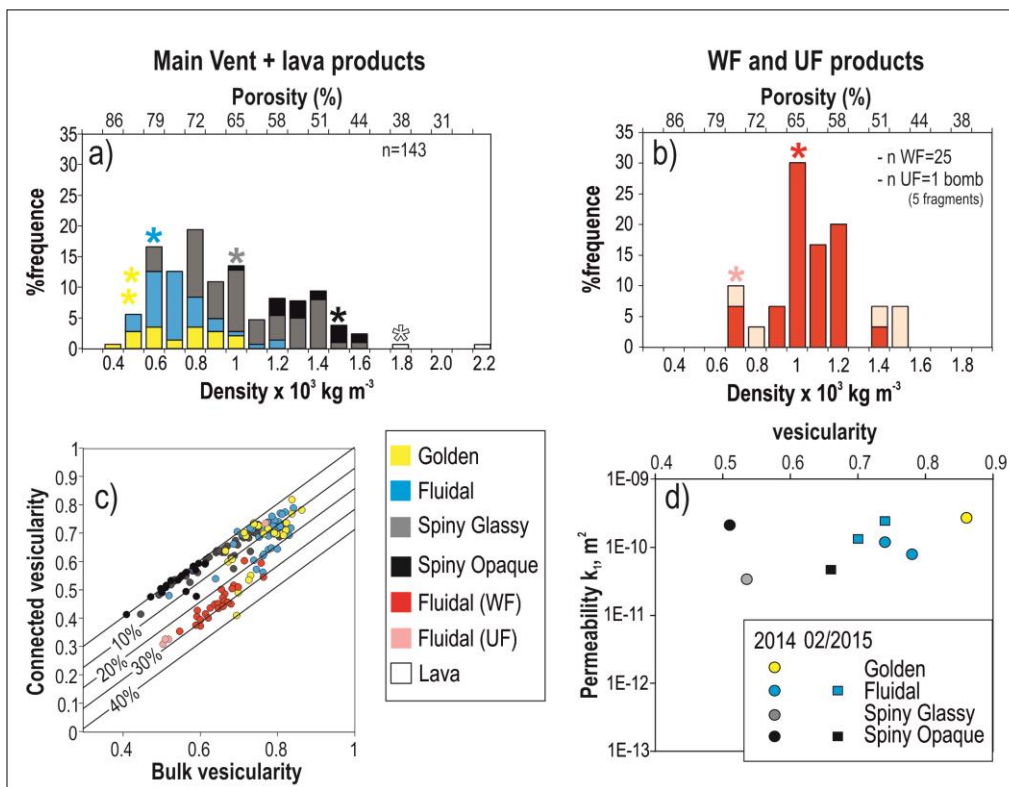
Figure 6 Density, connectivity and permeability data of June 2014 pyroclast and lava fragments: a) density distribution histogram for all the pyroclast fragments measured at the Main vent + two lava fragments collected from the Eastern front of the lava flow (see Fig. 1 for location). n = number of measured clasts; b) density distribution histogram for the pyroclasts sampled at the WF and the bomb sampled at the UF. The bomb broke in five fragments (2 fragments from the core, the least dense, and three fragments from the quenched edges, the densest); and c) In both the density the stars represent the density intervals from which we picked the clasts for the textural measurements; c) graph of connected vesicularity versus total vesicularity. The diagonal line represents equality between the connectivity and vesicularity, beneath this line the samples have isolated vesicles and the straight lines represent lines of equal fraction of isolated vesicles. To note that the bomb from the UF has the high vesicular core with less than 5% of isolated vesicles, while the three low vesicular fragments from the core have more than 25% of isolated vesicles; d) Darcian permeability (k_1) versus the vesicularity fraction. Data from June 2014 eruption and February 2015 eruption are reported.

Density and connectivity data of the 2014 pyroclast fragments: a) density distribution histogram for all the pyroclast fragments measured for the 2014 activity from the Main Vent; b) for the Western fracture; and c) for different typologies of clasts from the Main Vent; d) graph of connected vesicularity versus total vesicularity. The diagonal line represents equality between the connectivity and vesicularity, beneath this line the samples have isolated vesicles

1709
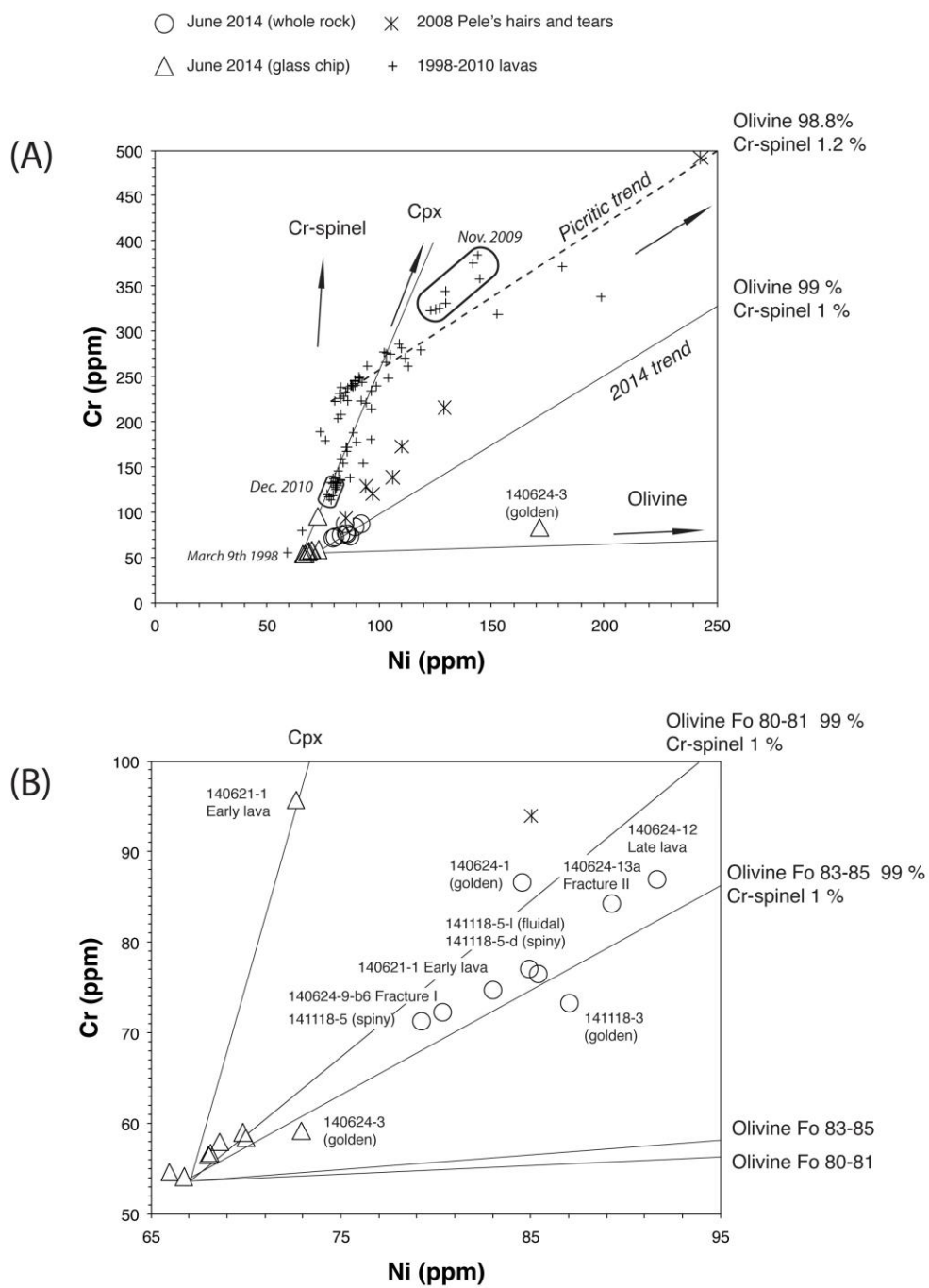
Figure 7 Ni-Cr concentration plot. (a) Ni-Cr signature of the June 2014 lavas compared to that of recent eruptions (Di Muro et al. (2015) and unpublished data). Whole-rock (circles)

and glass (triangles) compositions are shown for the June 2014 eruption. Olivine controlled lines are indicated for olivine hosting 1.2 and 0.6 wt.% Cr-spinel. Compositions used for olivine (Ni=1900 ppm, Cr=300ppm), clinopyroxene (Ni=970 ppm, Cr=4800 ppm), and Cr spinel (Ni=1500 ppm, Cr=25%) are inferred from Salaün et al. (2010), Di Muro et al. (2015) and Welsch et al. (2009). (b) Zoom of the Ni-Cr relationship between glass (triangles) and whole-rock (circles) samples from the June 2014 eruption. Fracture I = Western fracture, Fracture II = Upper fracture. Careful sample selection has permitted to obtain a set of virtually olivine-cpx free crystals. Any addition of mafic crystals translates into enrichment in Ni-Cr; those samples that contain a few % of crystals, (consistent with textural and petrological observation) are slightly enriched in compatible elements.
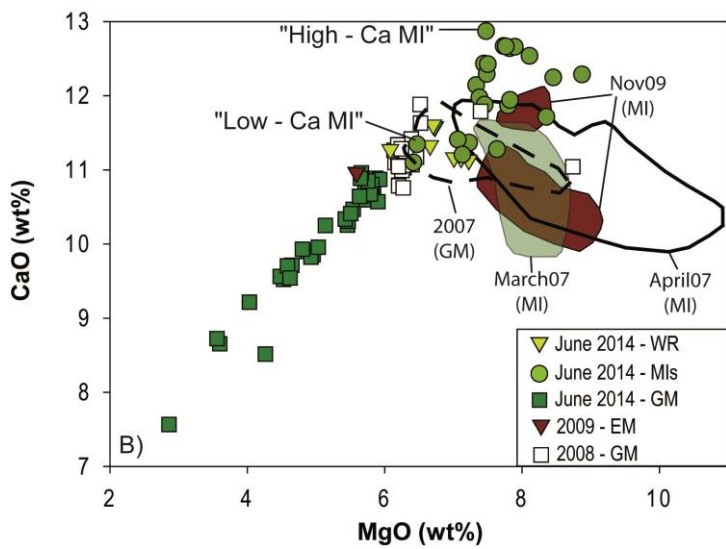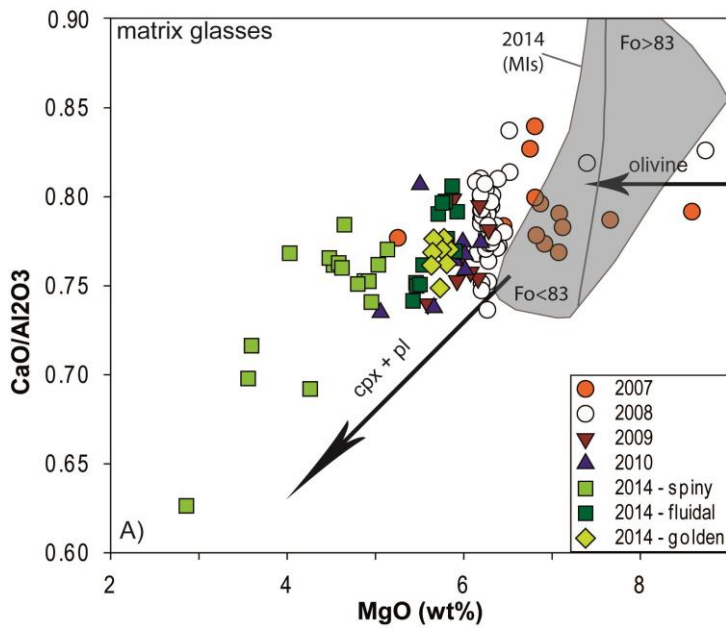
Fig. 8 (a) Evolution of CaO/Al$_2$O$_3$ ratio in the matrix glasses of recent eruptions at Piton de la Fournaise as a function of MgO content (directly proportional to melt temperature). MI = Melt inclusions (grey area for the 2014 samples). (b) CaO versus MgO content for Piton de la Fournaise products. WR = whole rock, GM = ground mass; MI = melt inclusion, EM = embayment glass
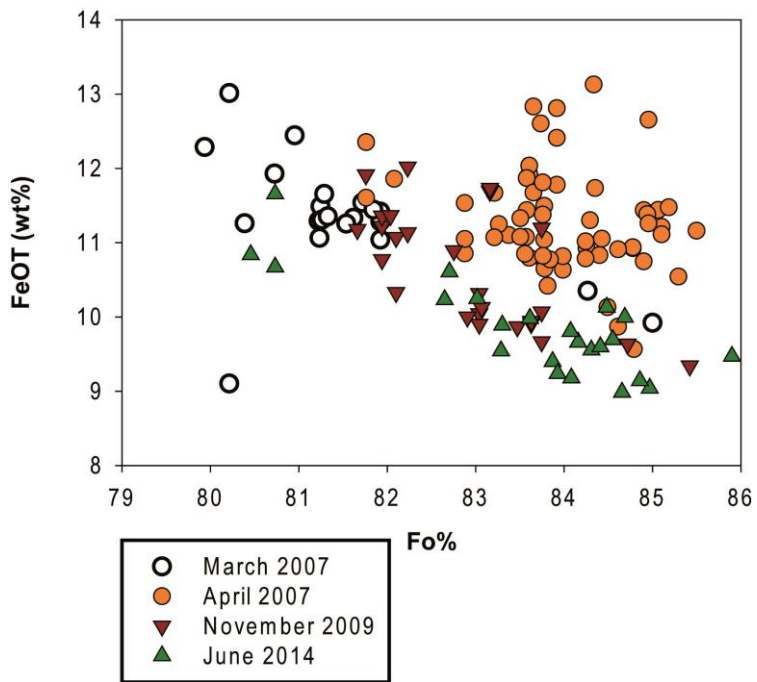
Figure 9 FeO_T in melt inclusions as function of Fo content of the olivine host for recent eruptions at Piton de la Fournaise

1731

1732

1733

1734

1735

1736

1737

1738

1739

1740

1741

1742

69
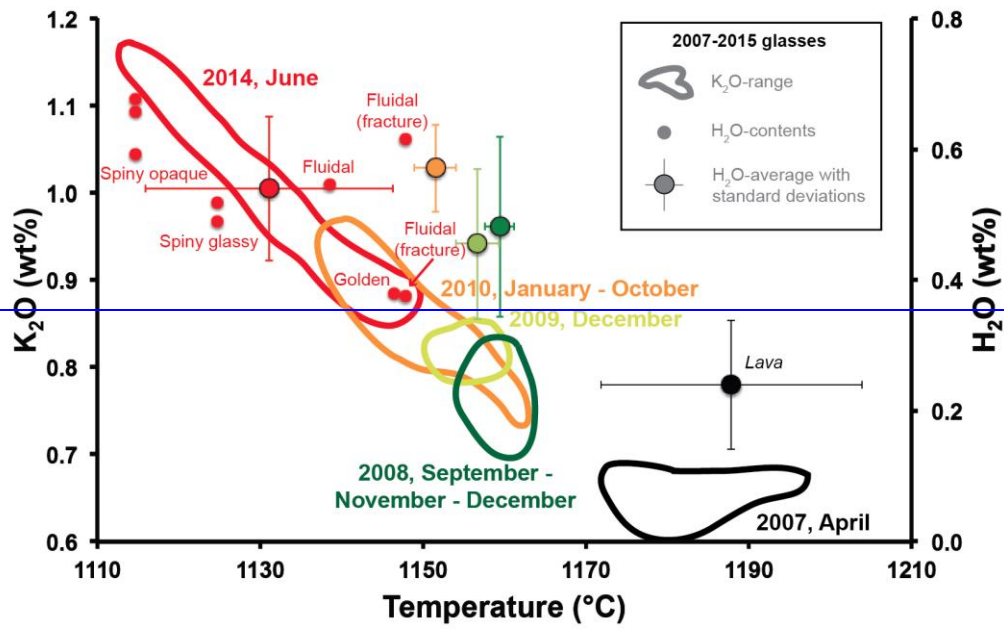
1743

1744
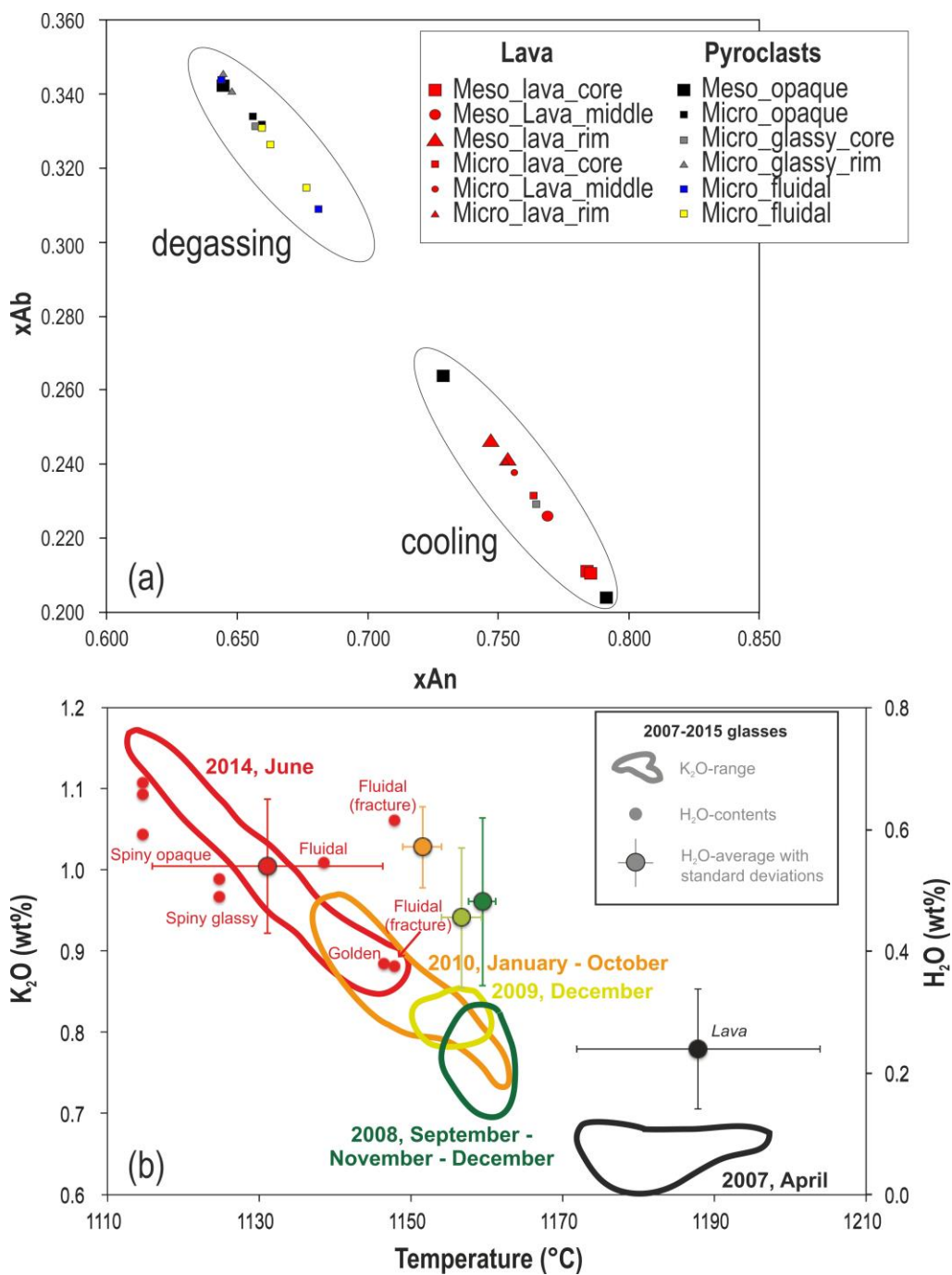
Figure 10 a) Anorthite versus Albite compositions for the plagioclase crystals measured for June 2014 eruption of PdF; b) Temperature, composition (K2O) and dissolved water content (H2O) for the evolution of 2007-2014 melts from glasses. The data have been obtained by

studying the glass-plagioclase equilibrium or on the basis of matrix glass analyses. Temperature estimation based on the MgO-thermometer of Helz and Thornber (1987) modified by Putirka (2008). Water content from the plagioclase hygrometer of Lange et al. (2009). Only plagioclases in equilibrium with melts are considered, following the procedure described by Putirka (2008) for >1050°C melts (Kd = 0.27±0.05). Error bars reported in Figure 10b correspond to the standard deviation of the plagioclase dataset, whose range is larger than error of the method. We stress that reported temperatures are obtained using Helz dry model; further uncertainty arises from the dependence of the method on dissolved water content as shown recently by Putirka (2008); in order to minimize the number of assumptions and perform a comparison between distinct eruptions, we preferred to adopt the dry model.
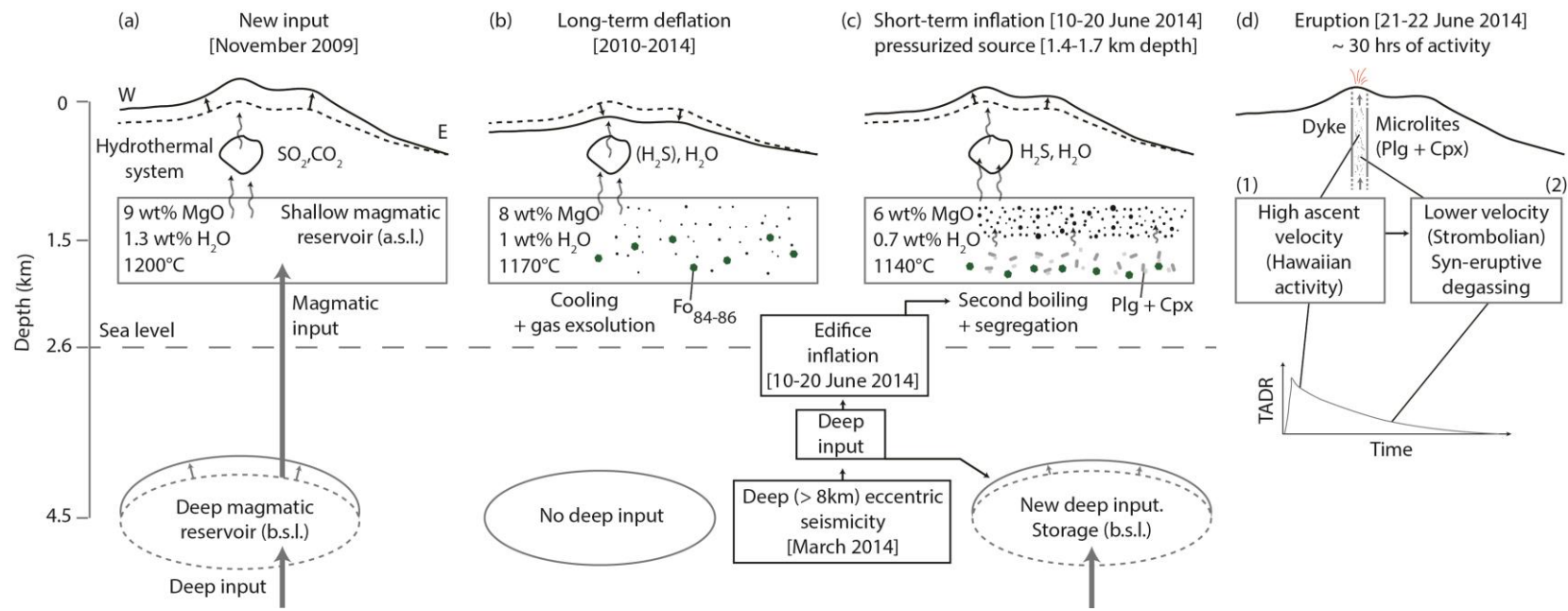
72
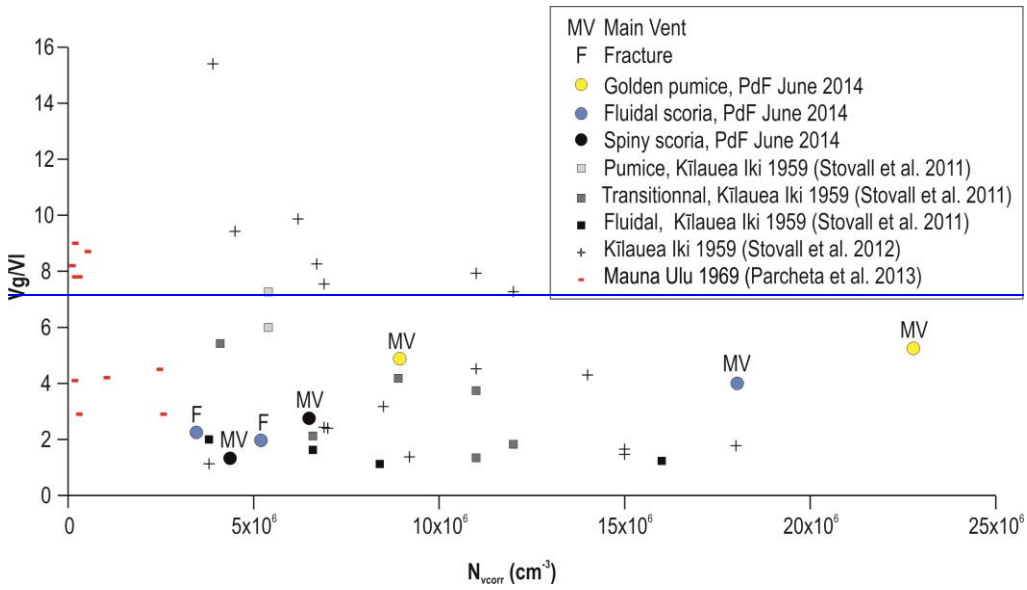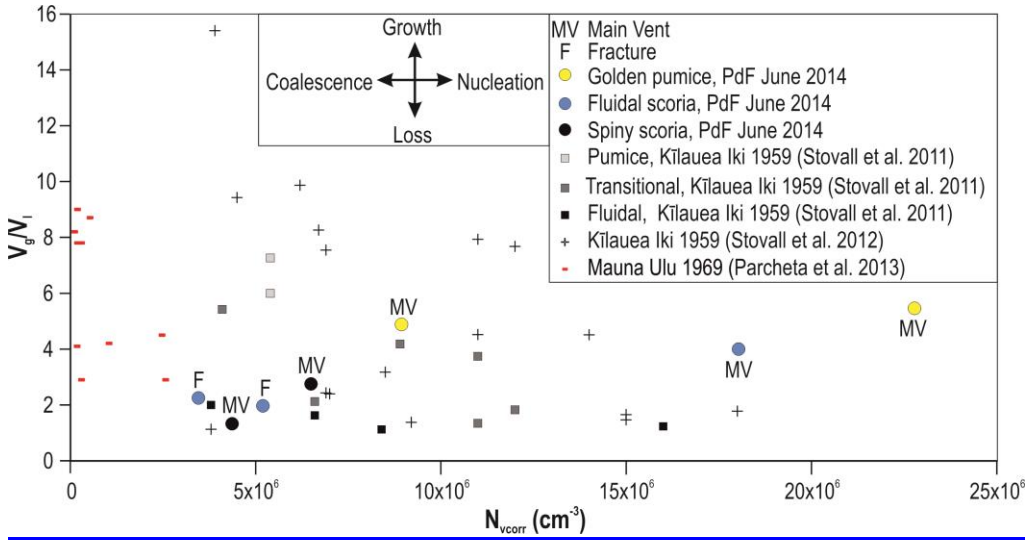
1781 **Figure 11** Volumetric ratio of vesicles to melt (V_G/V_L) versus vesicle number density

Figure 12 Schematic model of the evolution of PdF volcanic system from the new deep magmatic input of November 2009 up to June 2014 eruption. See explanation in the text

74